

# EVORA: Deep Evidential Traversability Learning for Risk-Aware Off-Road Autonomy

Xiaoyi Cai<sup>1</sup>, Siddharth Ancha<sup>1</sup>, Lakshay Sharma<sup>1</sup>, Philip R. Osteen<sup>2</sup>, Bernadette Bucher<sup>3</sup>, Stephen Phillips<sup>3</sup>, Jiuguang Wang<sup>3</sup>, Michael Everett<sup>4</sup>, Nicholas Roy<sup>1</sup>, and Jonathan P. How<sup>1</sup>

Project website: <https://xiaoyi-cai.github.io/evora>

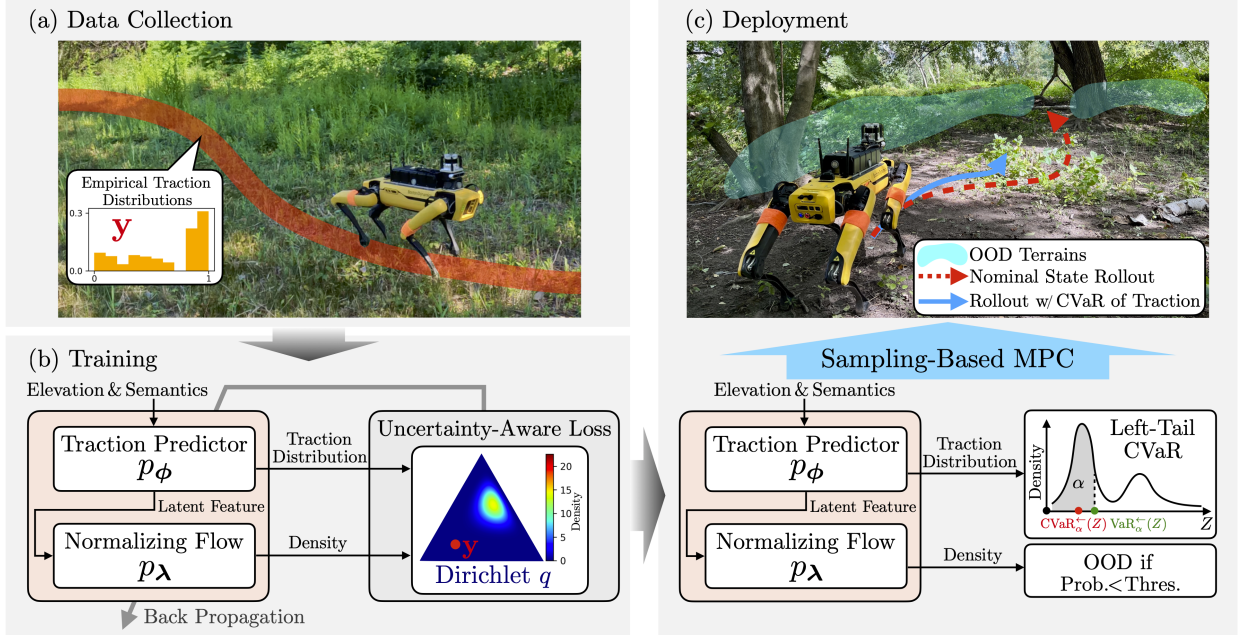


Fig. 1: Overview of the proposed *uncertainty-aware traversability learning* and *risk-aware navigation* methods. We use terrain *traction* as a measure of traversability. Intuitively, traction captures the “slip”, or the ratio between the commanded velocities and the achieved velocities. (a) We learn a traction model based on real-world data. The learned traction model contains *aleatoric uncertainty*, that is, the inherent and irreducible uncertainty due to partial observability, and *epistemic uncertainty* due to out-of-distribution inputs encountered at test time that are not well-represented in the training data. (b) Leveraging evidential deep learning [1], we learn categorical distributions over discretized traction values to capture aleatoric uncertainty and estimate epistemic uncertainty by using a normalizing flow network [2] to learn the densities of the traction predictor’s latent features. The overall architecture is trained with the proposed uncertainty-aware loss (21) defined for the Dirichlet distribution parameterized by the network outputs. (c) To handle aleatoric uncertainty, we propose a risk-aware planner that uses the left-tail conditional value at risk (CVaR) of the traction distribution to forward simulate the robot states when using the sampling-based model predictive control (MPC) method [3]. To handle epistemic uncertainty, we threshold the densities of the traction predictor’s latent features in order to identify and avoid out-of-distribution (OOD) terrain with unreliable traction predictions via auxiliary planning costs.

**Abstract**—Traversing terrain with good traction is crucial for achieving fast off-road navigation. Instead of manually designing costs based on terrain features, existing methods learn terrain properties directly from data via self-supervision, but challenges remain to properly quantify and mitigate risks due to uncertainties in learned models. This work efficiently quantifies both aleatoric and epistemic uncertainties by learning discrete traction distributions and probability densities of the traction predictor’s latent features. Leveraging evidential deep learning, we parameterize Dirichlet distributions with the network outputs and propose a novel uncertainty-aware squared Earth Mover’s distance loss with a closed-form expression that improves learning accuracy and navigation performance. The proposed risk-aware planner simulates state trajectories with the worst-case expected traction to handle aleatoric uncertainty, and penalizes trajectories

moving through terrain with high epistemic uncertainty. Our approach is extensively validated in simulation and on wheeled and quadruped robots, showing improved navigation performance compared to methods that assume no slip, assume the expected traction, or optimize for the worst-case expected cost.

## I. INTRODUCTION

Autonomous robots are increasingly being deployed in harsh off-road environments like mines, forests, and deserts [4]–[9], where both geometric and semantic understanding of the environments is required to identify non-geometric hazards (e.g., mud puddles, slippery surfaces) and geometric non-hazards (e.g., tall grass and foliage). To this end, recent approaches manually assign navigation costs based on semantic classification of the terrain [10]–[15], requiring significant human expertise to label and train a classifier sufficiently accurate and rich in order to achieve desired risk-aware behaviors. Alternatively, self-supervised learning can be used to learn a model of traversability directly from navigation data [16]–[18]. However, self-supervised data collection in the

<sup>1</sup>Massachusetts Institute of Technology, Cambridge, MA 02139, USA. {xyc, sancha, lakshays, nickroy, jhow}@mit.edu.

<sup>2</sup>DEVCOM Army Research Laboratory, Adelphi, MD 20783, USA. philip.r.osteen.civ@army.mil.

<sup>3</sup>Boston Dynamics AI Institute, Cambridge, MA 02142, USA. {bbucher, sphillips, jw}@theaiinstitute.com.

<sup>4</sup>Northeastern University, Boston, MA 02115, USA. m.everett@northeastern.edu.

real world can be slow and expensive. Furthermore, collecting more data is not beneficial unless we properly quantify and mitigate risks due to uncertainties in learned models. Uncertainty in learned models manifests in two forms. *Aleatoric uncertainty* is the inherent and irreducible uncertainty due to partial observability. For example, two different patches of terrain may be indistinguishable to the onboard sensors but lead to different vehicle behaviors—such uncertainty cannot be reduced by collecting more data. *Epistemic uncertainty* is due to out-of-distribution (OOD) inputs encountered at test time that are not well-represented in the training data. It is often undesirable to collect OOD data in dangerous situations such as collisions and falling at the edge of a cliff, so there can exist a large gap between training datasets and the various real-world scenarios encountered by the robot. Most existing work in off-road navigation has focused on either aleatoric uncertainty [19], [20] or epistemic uncertainty [21]–[24], but limited effort has been made to distinguish between both types of uncertainties to achieve fast and reliable off-road navigation.

Our proposed pipeline, **EVORA** (**E**Vidential **O**ff-**R**oad **A**utonomy), tightly integrates the solutions to the upstream *uncertainty-aware traversability learning* problem and the downstream *risk-aware navigation* problem for off-road navigation (see Fig. 1 for an overview). To plan fast trajectories, we model traversability with terrain *traction* that captures the “slip” or the ratio between the commanded velocities and the achieved velocities (for example, wet terrain that causes the robot’s wheels to slip and reduce its intended velocity has low traction). Moreover, we efficiently quantify both aleatoric and epistemic uncertainties by learning the empirical traction distributions and probability densities of the traction predictor’s latent features. Because real world traction distributions may be non-Gaussian (see examples in Fig. 17 and Fig. 20), we learn categorical distributions over discretized traction values to capture multi-modality. By leveraging the evidential deep learning technique proposed in [1], we parametrize Dirichlet distributions (the conjugate priors for the categorical distributions) with neural network (NN) outputs, and propose a novel uncertainty-aware loss based on the squared Earth Mover’s distance [25]. Our loss, which can be computed efficiently in closed-form, better captures the relationship among discretized traction values than the conventional cross entropy-based losses [1], [26]. To handle aleatoric uncertainty, we propose a risk-aware planner that simulates state trajectories using the worst-case expected traction. The proposed method is shown to outperform state-of-the-art methods that rely on the nominal traction [20], the expected traction [27] or that optimize for the worst-case expected cost [28]. To mitigate the risk due to epistemic uncertainty, the proposed method imposes a confidence threshold on the densities of the traction predictor’s latent space features in order to identify OOD terrain and avoid moving through it using auxiliary planning costs. The overall approach is extensively analyzed in simulation and hardware with wheeled and quadruped robots, demonstrating feasibility and improved navigation performance in practice.

## A. Related Work

Traversability analysis can be achieved in various ways, e.g., based on proprioceptive measurements [29], [30], geometric features [6], [7], [31] and combination of geometric and semantic features [9], [10], [32]–[34] (see the survey in [35]). Due to the difficulty of hand-crafting planning costs based on terrain features, self-supervised learning is increasingly being adopted to learn task-relevant traversability representations. For example, support surfaces underneath dense vegetation can be learned for legged robot locomotion [36], and terrain traction can be learned to capture how well the robot can follow the desired velocities for planning fast trajectories [27]. However, these methods do not account for the aleatoric and epistemic uncertainties due to the noisiness and scarcity of real-world data. To capture aleatoric uncertainty, methods such as [19], [20] learn multi-modal terrain properties via Gaussian mixture models or categorical distributions. To capture epistemic uncertainty, methods such as [21], [22], [37] measure the trained NNs’ ability to reconstruct terrain similar to the terrain types traversed in the past, and [38] trains a binary classification network for unfamiliar terrain. In comparison, techniques based on Gaussian Process (GP) regression [23], [24] capture epistemic uncertainty but they use a homoscedastic noise model that assumes the noise variance is globally constant. While heteroscedastic GPs that can handle input-dependent noise exist [39], the predictive distributions are not analytically tractable and require approximations. In contrast, our work explicitly quantifies both the aleatoric and the epistemic uncertainties and tightly integrates the uncertainty-aware traversability model with downstream risk-aware planners.

While the uncertainty of the learned traversability model can be quantified, challenges remain regarding how to properly handle uncertainty in the downstream planner to generate risk-aware behaviors. Risk due to undesirable terrain types can be represented as costmaps [20], [40], [41], where Conditional Value at Risk (CVaR) can be used to measure the cost of encountering worst-case expected failures, which satisfies a group of axioms important for rational risk assessment [42]. Instead of using costmaps, navigation performance can be assessed based on the expected future states [43] or the expected terrain parameters [27]. However, these methods rely on either the nominal or the expected system behavior, which may provide a poor indication of the actual system performance when the vehicle-terrain interaction is noisy. As proposed in [28], the CVaR of the planning objective can be optimized by evaluating each control sequence over samples of noisy terrain traction, but this approach is computationally expensive. The recent work of [44] quantifies both aleatoric and epistemic uncertainties using probabilistic ensembles [45] and plans risk-aware trajectories by assigning penalties for both types of uncertainties. However, it relies on the expected system parameters for forward simulation. While we adopt a similar strategy for handling epistemic uncertainty via auxiliary penalties, we use the worst-case expected system parameters for forward simulation to assess the risk due to aleatoric uncertainty. Compared to [27], [44], our method produces behaviors more robust to multi-modal

terrain properties observed in the real world.

Uncertainty quantification is well studied in the machine learning literature (see the survey in [46]) with effective techniques such as Bayesian dropout [47], model ensembles [48], and evidential methods [1]. In the off-road navigation literature, ensemble methods have been a popular choice [41], [44], [49], because they typically outperform methods based on Bayesian dropout [50]. In comparison, evidential methods are better suited for real-world deployment, because they only require a single network evaluation without imposing high computation or memory requirements. Therefore, we leverage the evidential method proposed in [1] that directly parameterizes the conjugate prior distribution of the target distribution with NN outputs. Specifically, we model the target traction distributions as categorical distributions to capture aleatoric uncertainty, which imply Dirichlet conjugate priors whose concentration parameters, determined by the densities of the traction predictor’s latent features, provide information about epistemic uncertainty. We improve upon [1] by proposing an uncertainty-aware loss based on the squared Earth Mover’s Distance [25]. Our loss can be computed efficiently in closed-form and better captures the relationship among the discrete traction values, resulting in more accurate traction predictions that in turn improve the downstream risk-aware planner’s navigation performance.

### B. Contributions

This work proposes an off-road navigation pipeline that tightly integrates the solutions to the uncertainty-aware traversability learning problem and the risk-aware motion planning problem. We explicitly quantify both the epistemic uncertainty to understand when the predicted traction values are unreliable due to novel terrain and the aleatoric uncertainty to enable the downstream planner to mitigate risk due to noisy traction estimates. The main contributions of this work are:

- 1) A probabilistic traversability model based on traction distributions (aleatoric uncertainty), with the ability to identify unreliable predictions via the densities of the traction predictor’s latent features (epistemic uncertainty).
- 2) A novel uncertainty-aware loss based on the squared Earth Mover’s Distance (EMD<sup>2</sup> [25]) with a closed-form expression derived in this work that improves traction prediction accuracy, OOD detection performance, and downstream navigation performance when used together with the uncertainty-aware cross entropy loss [1].
- 3) A risk-aware planner based on the CVaR of traction to handle aleatoric uncertainty. Our planner outperforms state-of-the-art methods that assume the nominal traction [20], the expected traction [27], or that optimize for the CVaR of cost [28] both in simulation and hardware.
- 4) A further extension of the risk-aware planner to handle epistemic uncertainty by avoiding OOD terrain with unlikely latent features. This approach improves the navigation success rate in simulation and reduces the number of human interventions required in hardware experiments.

The preliminary conference version of this work appeared in [51], which proposed the idea of learning traction distributions and the risk-aware cost formulations based on CVaR;

however, experiments were only performed in simulation. This work extends the prior work by: (1) reducing the reliance on the cross entropy loss for learning traction distributions (shown to perform poorly when the target bins have strong relationships [25]), and (2) eliminating the disjoint training of the traction predictor and the latent space density estimator (shown to limit the learning performance [1]). We leverage the evidential learning technique proposed in [1] to jointly train the overall network with a newly derived uncertainty-aware EMD<sup>2</sup> loss [25]. This loss better captures cross-bin relationships of discretized traction values. The new methods introduced in this work not only improve the accuracies of traction prediction and OOD detection but also leads to faster navigation. By adding extensive indoor and outdoor hardware experiments, this paper provides stronger evidence of the performance improvements provided by the risk-aware planner proposed in the conference version [51] compared to the state-of-the-art methods [20], [27], [28].

## II. PROBLEM FORMULATION

We consider the problem of motion planning for a ground vehicle whose dynamics depend on the terrain traction. Because traction values can be uncertain in the presence of rough terrain and imperfect sensing, we model traction values as random variables whose distributions can be estimated from sensor data using a learned model. Next, we will introduce the dynamical models under consideration and the formulation of the motion planning problem.

### A. Dynamical Models with Uncertain Traction Parameters

Consider the discrete time system:

$$\mathbf{x}_{t+1} = F(\mathbf{x}_t, \mathbf{u}_t, \boldsymbol{\psi}_t), \quad (1)$$

where  $\mathbf{x}_t \in \mathbf{X} \subseteq \mathbb{R}^n$  is the state vector such as the position and orientation of the robot,  $\mathbf{u}_t \in \mathbb{R}^m$  is the control input provided to the robot, and  $\boldsymbol{\psi}_t \in \boldsymbol{\Psi} \subseteq \mathbb{R}^r$  is the parameter vector that captures properties of the terrain such as traction. We consider two models that are useful approximations of the dynamics of a wide range of robots as shown in Fig. 2. Applicable to both differential-drive and legged robots, the **unicycle model** is defined as:

$$\begin{bmatrix} p_{t+1}^x \\ p_{t+1}^y \\ \theta_{t+1} \end{bmatrix} = \begin{bmatrix} p_t^x \\ p_t^y \\ \theta_t \end{bmatrix} + \Delta \cdot \begin{bmatrix} \psi_1 \cdot v_t \cdot \cos(\theta_t) \\ \psi_1 \cdot v_t \cdot \sin(\theta_t) \\ \psi_2 \cdot \omega_t \end{bmatrix}, \quad (2)$$

where  $\mathbf{x}_t = [p_t^x, p_t^y, \theta_t]^\top$  contains the X, Y positions and yaw,  $\mathbf{u}_t = [v_t, \omega_t]^\top$  contains the commanded linear and angular velocities,  $\boldsymbol{\psi}_t = [\psi_1, \psi_2]^\top$  contains the linear and angular traction values  $0 \leq \psi_1, \psi_2 \leq 1$ , and  $\Delta > 0$  is the time interval. Intuitively, traction captures the “slip”, or the ratio between the commanded velocities and the achieved velocities. The **bicycle model** is applicable for Ackermann-steering robots and is defined as

$$\begin{bmatrix} p_{t+1}^x \\ p_{t+1}^y \\ \theta_{t+1} \end{bmatrix} = \begin{bmatrix} p_t^x \\ p_t^y \\ \theta_t \end{bmatrix} + \Delta \cdot \begin{bmatrix} \psi_1 \cdot v_t \cdot \cos(\theta_t) \\ \psi_1 \cdot v_t \cdot \sin(\theta_t) \\ \psi_2 \cdot v_t \cdot \tan(\delta_t)/L \end{bmatrix}, \quad (3)$$

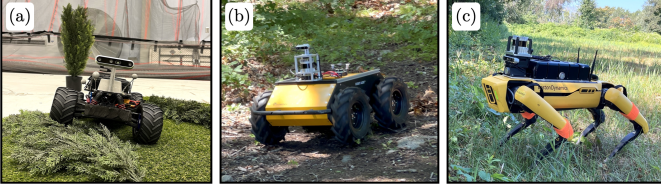


Fig. 2: Example ground robots that can be modeled with unicycle or bicycle dynamics models. (a) RC car. (b) Differential-drive robot. (c) Legged robot.

where  $L$  is the wheelbase,  $\mathbf{u}_t = [v_t, \delta_t]^\top$  contains the commanded linear velocity and steering angle, and  $\psi_t$  plays the same role as in the unicycle model. The reference point for the bicycle model in (3) is located at the center between the two rear wheels.

### B. Motion Planning

As this work focuses on fast navigation to the goal, we adopt the minimum-time objective used in [20], but other objectives can also be used. Intuitively, the objective only assigns stage costs by accumulating the elapsed time before any state falls in the goal region. If the state trajectory does not intercept the goal region, the terminal cost further penalizes the estimated time-to-goal. Given initial state  $\mathbf{x}_0$  and a function  $C^{\text{dist}}(\mathbf{x}_t)$  that measures the Euclidean distance between  $\mathbf{x}_t$  and the goal, we want to find a control sequence  $\mathbf{u}_{0:T-1}$  that solves

$$\min_{\mathbf{u}_{0:T-1}} C(\mathbf{x}_{0:T}) := C^{\text{term}}(\mathbf{x}_T) + \sum_{t=0}^{T-1} C^{\text{stage}}(\mathbf{x}_t), \quad (4)$$

$$\text{s.t. } \mathbf{x}_{t+1} = F(\mathbf{x}_t, \mathbf{u}_t, \psi_t), \quad \forall t \in \{0, \dots, T-1\}, \quad (5)$$

where the total cost consists of terminal and stage costs:

$$C^{\text{term}}(\mathbf{x}_T) = \frac{C^{\text{dist}}(\mathbf{x}_T)}{s^{\text{default}}} (1 - \mathbb{1}^{\text{done}}(\mathbf{x}_{0:T})), \quad (6)$$

$$C^{\text{stage}}(\mathbf{x}_t) = \Delta (1 - \mathbb{1}^{\text{done}}(\mathbf{x}_{0:t})), \quad (7)$$

where  $s^{\text{default}} > 0$  is the default speed for estimating time-to-go and  $\Delta > 0$  is the constant time interval. To avoid accumulating costs after arrival at the goal, we use an indicator function  $\mathbb{1}^{\text{done}}(\mathbf{x}_{0:t})$  that equals 1 if any state in  $\mathbf{x}_{0:t}$  has reached the goal, and equals 0 otherwise. Although  $\Delta$  is a constant, the number of time steps required to reach the goal changes according to the robot speed. Intuitively, this objective encourages the robot to reach the goal as quickly as possible.

### C. Key Challenges

While the problem (4) can be optimized via nonlinear optimization techniques such as Model Predictive Path Integral control (MPPI [3, Algorithm 2]), the terrain traction  $\psi$  varies across terrain types and needs to be learned from real-world navigation data. However, real-world terrain traction is uncertain since visually and geometrically similar terrain may have different traction properties (aleatoric uncertainty), and the traction models can only be trained on limited data (epistemic uncertainty). Even if uncertainty in terrain traction is quantified accurately, designing risk-aware planners that mitigate the risk of failures under this uncertainty is still a remaining challenge. To address these challenges, we introduce our proposed uncertainty-aware traversability model and the risk-aware planner in Sec. III and Sec. IV, respectively.

## III. UNCERTAINTY-AWARE TRAVERSABILITY MODEL

In this section, we first introduce the traction distribution predictor that captures the aleatoric uncertainty, and the latent space density estimator that captures epistemic uncertainty. An overview of the traversability analysis pipeline is shown in Fig. 3. Then, we review how to parameterize Dirichlet distributions with NN outputs according to [1] and propose the new uncertainty-aware squared Earth Mover’s Distance loss that better captures cross-bin relationships among discretized traction values compared to the uncertainty-aware cross entropy loss proposed in [1] for classification tasks.

### A. Aleatoric Uncertainty Captured in Traction Distribution

Given the set of system parameters  $\psi \in \Psi$  with  $B > 0$  discretized values  $\Psi = \{\psi^1, \dots, \psi^B\}$ , we want to model the distribution over  $\Psi$  conditioned on terrain features  $\mathbf{o} \in \mathcal{O}$ :

$$p_\phi(\mathbf{o}) : \mathcal{O} \rightarrow \mathbb{R}_{\geq 0}^B, \quad (8)$$

where  $\text{Cat}(p_\phi(\mathbf{o}))$  is a categorical distribution over  $\Psi$ , and (8) can be learned by an NN parameterized by  $\phi$  that can be trained using an empirically collected dataset  $\{(\mathbf{o}, \psi)_k\}_{k=1}^K$  where  $K > 0$ . Every terrain feature  $\mathbf{o} \in \mathcal{O}$  consists of the terrain elevation measured in meter and the one-hot encoding of the semantic label. While we only consider “dirt” and “vegetation” semantic types in simulation, more fine-grained semantic labels are needed in practice. A real world example can be found in Fig. 4 where a Clearpath Husky with the unicycle model was manually driven in a forest to build an environment model and collect traction data. The semantic and geometric information about the environment can be built by using a semantic octomap [52] that temporally fuses semantic point clouds. We used PointRend [53] trained on the RUGD off-road navigation dataset [54] with 24 semantic categories to segment RGB images and subsequently projected the semantics onto lidar point clouds.

*Remark 1.* Categorical distributions are convenient alternatives to Gaussian Mixture Models and normalizing flows [2] for learning multi-modal traction distributions observed in practice (see Sec. IX), because they do not require tuning the number of clusters, generate bounded distributions by construction, and converge faster than normalizing flows based on our empirical experience while achieving similar accuracy. However, choosing the correct discretization levels may be challenging and the total number of bins grow exponentially with the variables’ dimensions. Therefore, categorical distributions may not be suitable for high-dimensional systems, but they suffice for our use case where we only consider linear and angular traction values with a relatively low number of discrete bins.

### B. Epistemic Uncertainty Captured in Latent Space Density

Due to limited training data, the predicted traction distributions for novel parts of the terrain may be unreliable and lead to degraded navigation performance in those regions. To measure epistemic uncertainty, we want to estimate the density of the latent feature  $\mathbf{z}_\mathbf{o} \in \mathbb{R}^H$  obtained from an intermediate



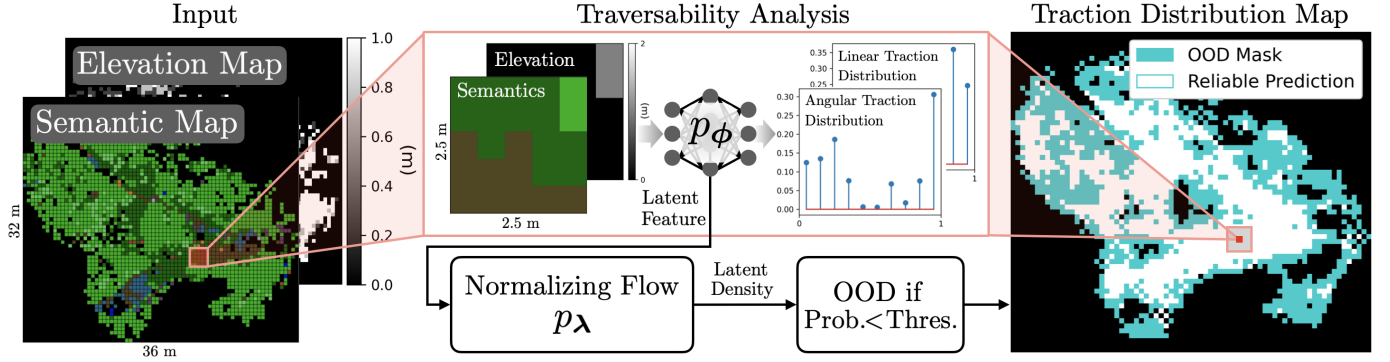


Fig. 3: The proposed traversability pipeline maps elevation and semantic features to traction distributions that capture aleatoric uncertainty, and density for latent features that capture epistemic uncertainty. Terrain regions are deemed out-of-distribution (OOD) and later avoided during planning if the densities for the latent features are below a threshold. When the densities for latent features are above the threshold, the predicted traction distributions are reliable and inform downstream risk-aware planners (Sec. IV) to trade off the risk of immobilization with the time savings by traversing regions with uncertain traction.

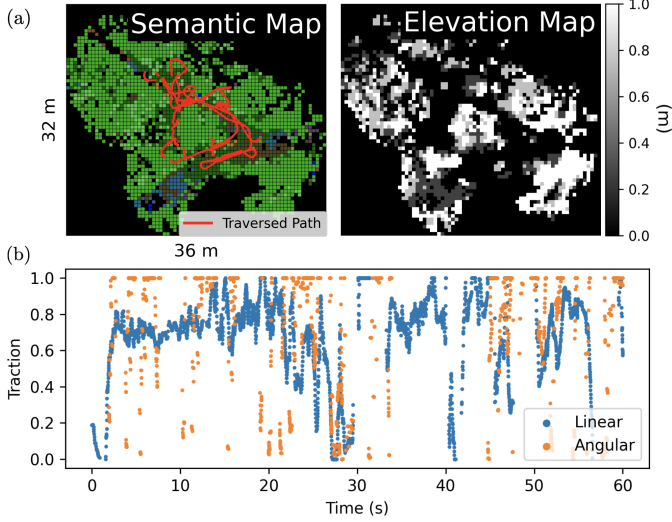


Fig. 4: Real world traction data collected using a Clearpath Husky. (a) The robot was manually driven for 10 minutes while building a semantic octomap, from which a projected 2D semantic map and an elevation map can be extracted. Example terrain types include vegetation (light green), grass (dark green), and mulch (brown). (b) Only a subset of the collected linear and angular traction values are shown for clarity. Note that discontinuity in traction values occurred when linear or angular commands were not sent.

layer of the traction predictor  $p_{\phi}$  (8) based on the terrain feature  $\mathbf{o}$ . The density estimator is defined as:

$$p_{\lambda}(\mathbf{z}_{\mathbf{o}}) : \mathbb{R}^H \rightarrow \mathbb{R}_{\geq 0}, \quad (9)$$

where we use a normalizing flow parameterized by  $\lambda$  to learn (9), because normalizing flows are differentiable and can be optimized via gradient descent. At a high level, a normalizing flow works by transforming an arbitrary target distribution into a simple base distribution such as a standard normal via a sequence of invertible and differentiable mappings. Therefore, the density of a sample can be computed by multiplying the density of the transformed sample under the base distribution and the change in volume measured by the product of the absolute values of the determinants of the Jacobians for each transformation via the change of variable formula [2].

We design a simple confidence score  $g_{\mathbf{o}}$  for input feature  $\mathbf{o}$  based on the maximum density  $p^{\max} \in \mathbb{R}_{\geq 0}$  and minimum density  $p^{\min} \in \mathbb{R}_{\geq 0}$  observed for the latent features of terrain

in the training dataset:

$$g_{\mathbf{o}} = \frac{p_{\lambda}(\mathbf{z}_{\mathbf{o}}) - p^{\min}}{p^{\max} - p^{\min}}, \quad (10)$$

where  $g_{\mathbf{o}}$  is not necessarily limited to  $[0, 1]$  and lower values indicate that terrain features are less similar to the training data. During deployment, terrain features with a confidence score below a tuned threshold  $g^{\text{thres}}$  are deemed OOD; these regions with OOD terrain features can be explicitly avoided during planning via auxiliary penalties. This strategy improves navigation success rate when the NN is deployed in an environment unseen during training (see Sec. VIII and Sec. IX-B).

### C. Evidential Deep Learning

While the traction predictor and the density estimator can be trained sequentially, the existing work [1] has shown that joint training using evidential deep learning techniques can improve OOD detection performance while retaining similar prediction accuracy. In this section, we review the method proposed in [1] that parameterizes Dirichlet distributions (the conjugate priors of categorical distributions) with NN outputs, and the uncertainty-aware cross entropy loss that provides regularization for the latent space.

The Dirichlet distribution  $q = \text{Dir}(\beta)$  with the concentration parameter  $\beta \in \mathbb{R}_{\geq 0}^B$  is a distribution over categorical distributions  $\text{Cat}(\mathbf{p})$ , where  $\mathbf{p} \in \mathbb{R}_{\geq 0}^B$  is a probability mass function (PMF) over  $B > 0$  bins and  $\mathbf{p} \sim \text{Dir}(\beta)$ . Given a prior Dirichlet belief  $\text{Dir}(\beta^{\text{prior}})$ , input feature  $\mathbf{o}$  and the associated latent feature  $\mathbf{z}_{\mathbf{o}} \in \mathbb{R}^H$ , the NN performs an input-dependent posterior update that leads to the expected PMF:

$$\mathbf{p}_{\mathbf{o}}^{\text{post}} = \frac{n^{\text{prior}} \mathbf{p}^{\text{prior}} + n_{\mathbf{o}} p_{\phi}(\mathbf{o})}{n^{\text{prior}} + n_{\mathbf{o}}}, \quad (11)$$

where  $p_{\phi}(\mathbf{o})$  is the PMF prediction conditioned on the terrain feature  $\mathbf{o}$ , and  $n_{\mathbf{o}} = N_H p_{\lambda}(\mathbf{z}_{\mathbf{o}})$  is the total evidence based on the certainty budget  $N_H > 0$  and the density for the latent feature  $p_{\lambda}(\mathbf{z}_{\mathbf{o}})$ . Without prior information, we set  $n^{\text{prior}} = B$  and  $\mathbf{p}^{\text{prior}} = \mathbb{1}_B / B$ , where  $\mathbb{1}_B \in \mathbb{R}^B$  is a vector of all ones.  $\text{Dir}(\beta^{\text{prior}})$  then corresponds to a uniform distribution over all PMFs. Given the target PMF  $\mathbf{y} \in \mathbb{R}_{\geq 0}^B$  that contains the empirically estimated traction distribution, the traction

predictor and the normalizing flow can be trained jointly with the following uncertainty-aware cross entropy (UCE) loss [1]:

$$\min_{\phi, \lambda} L^{\text{UCE}}(q, \mathbf{y}) - H(q), \quad (12)$$

where  $L^{\text{UCE}}(q, \mathbf{y})$  is defined as the expected cross entropy loss given the predicted Dirichlet  $q$ :

$$L^{\text{UCE}}(q, \mathbf{y}) := \mathbb{E}_{\mathbf{p} \sim q} \left[ - \sum_{b=1}^B y_b \log p_b \right] \quad (13)$$

$$= - \sum_{b=1}^B y_b (\Psi(\beta_b) - \Psi(\beta_0)) \quad (14)$$

where  $\Psi$  is the digamma function,  $\beta_0 := \sum_{b=1}^B \beta_b$  is the overall evidence, and  $H(q)$  is an entropy term that encourages smoothness in the latent space of the traction predictor:

$$H(q) = \log \mathcal{B}(\beta) + (\beta_0 - B) \Psi(\beta_0) - \sum_{b=1}^B (\beta_b - 1) \Psi(\beta_b), \quad (15)$$

where  $\mathcal{B}$  denotes the beta function. The ablation study in [1] has shown that jointly training  $p_\phi$  and  $p_\lambda$  with (12) improves OOD detection performance while retaining similar accuracy obtained from training  $p_\phi$  with the conventional cross entropy (CE) loss. However, the key limitation of CE-based losses in our use case is that they treat the prediction errors across bins independently. The independence assumption is undesirable for learning traction where bins are obtained by discretizing continuous traction values. These bins are ordered—bins closer to each other should be treated more similarly than bins far apart. We address this limitation by proposing a new loss function based on the squared Earth Mover's Distance [25] that has been shown to achieve better accuracy than CE-based losses when bins are ordered.

#### D. Uncertainty-Aware Squared Earth Mover's Distance

Intuitively the Earth Mover's Distance (EMD) between two distributions measures the minimum cost of transporting the probability mass of one distribution to the other, which has a closed-form solution for two categorical distributions defined by PMFs with the same number of bins [25]. Given a predicted PMF  $\mathbf{p} \in \mathbb{R}_{\geq 0}^B$  and the target  $\mathbf{y} \in \mathbb{R}_{\geq 0}^B$ , the normalized EMD with  $l$ -norm for  $B$  equally-spaced bins can be computed in closed-form [25]:

$$\text{EMD}(\mathbf{p}, \mathbf{y}) = \left( \frac{1}{B} \right)^{\frac{1}{l}} \|\text{cs}(\mathbf{p}) - \text{cs}(\mathbf{y})\|_l, \quad (16)$$

where  $\text{cs} : \mathbb{R}^B \rightarrow \mathbb{R}^B$  is the cumulative sum operator. For convenience during training, we use  $l = 2$  for Euclidean distance and optimize the squared EMD loss ( $\text{EMD}^2$ ), dropping the constant factor. The toy example in Fig. 6 clearly shows that  $\text{EMD}^2$  better captures the physical meaning of the predicted PMFs than CE which ignores the relationship between bins.

As  $\text{EMD}^2$  is only defined for PMFs, a naïve strategy is to compare the target  $\mathbf{y}$  to the expected PMF from the predicted Dirichlet  $q$ , which leads to the following loss function (ignoring the constant multiplicative term):

$$\begin{aligned} L^{\text{EMD}^2}(q, \mathbf{y}) &:= \|\text{cs}(\bar{\mathbf{p}}) - \text{cs}(\mathbf{y})\|_2^2, \\ &= \text{cs}(\bar{\mathbf{p}})^\top \text{cs}(\bar{\mathbf{p}}) + \eta(q, \mathbf{y}), \end{aligned} \quad (17)$$

where  $\bar{\mathbf{p}} := E_{\mathbf{p} \sim q}[\mathbf{p}] = \beta/\beta_0$  is the expected PMF and

$$\eta(q, \mathbf{y}) := -2 \text{cs}(\bar{\mathbf{p}})^\top \text{cs}(\mathbf{y}) + \text{cs}(\mathbf{y})^\top \text{cs}(\mathbf{y}). \quad (18)$$

Note that  $\text{cs}(\bar{\mathbf{p}})$  can also be written as  $\text{cs}(\beta)/\beta_0$  due to the linearity of the cumulative sum operator. However,  $L^{\text{EMD}^2}$  is invariant to the concentration parameters  $\beta$  of the Dirichlet distribution, as illustrated in the toy example in Fig. 5, so the epistemic uncertainty cannot be learned accurately.

Similar to the approach in [1] that uses the expectation of the cross entropy loss (13) that depends on  $\beta$ , we propose the uncertainty-aware  $\text{EMD}^2$  ( $\text{UEMD}^2$ ) loss defined as the expectation of the  $\text{EMD}^2$  given the Dirichlet  $q$ :

$$L^{\text{UEMD}^2}(q, \mathbf{y}) := \mathbb{E}_{\mathbf{p} \sim q} [\text{EMD}^2(\mathbf{p}, \mathbf{y})]. \quad (19)$$

The following theorem states that our proposed  $\text{UEMD}^2$  loss can be computed in a closed form.

*Theorem 1: Closed-form expression for  $\text{UEMD}^2$  loss*

Let  $q = \text{Dir}(\beta)$  be a Dirichlet distribution and let  $\text{Cat}(\mathbf{y})$  be a categorical distribution. Then, a closed-form expression exists for  $L^{\text{UEMD}^2}(q, \mathbf{y})$  given by:

$$L^{\text{UEMD}^2}(q, \mathbf{y}) = \text{cs}(\bar{\mathbf{p}})^\top \frac{\text{cs}(\beta) + \mathbb{1}_B}{\beta_0 + 1} + \eta(q, \mathbf{y}) \quad (20)$$

where  $\bar{\mathbf{p}} = \mathbb{E}_{\mathbf{p} \sim q}[\mathbf{p}]$ , and  $\eta$  is defined in (18).

*Proof.* See Appendix A.  $\square$

Due to structural similarity with  $L^{\text{EMD}^2}$  (17), the proposed loss (20) also penalizes the  $\text{EMD}^2$  error to encourage accurate traction predictions. In addition, the proposed loss penalizes low concentration  $\beta$  to encourage low epistemic uncertainty as shown in Fig. 5. In fact, it can be proved that  $L^{\text{UEMD}^2}$  is always greater or equal to  $L^{\text{EMD}^2}$  using Jensen's inequality and the convexity<sup>1</sup> of  $L^{\text{EMD}^2}$ . To prevent the overall evidence from increasing infinitely, we also apply entropy regularization (15). To leverage the benefits of both UCE and  $\text{UEMD}^2$ , we consider the following multi-objective optimization:

$$\min_{\phi, \lambda} w_1 L^{\text{UCE}}(q, \mathbf{y}) + w_2 L^{\text{UEMD}^2}(q, \mathbf{y}) - w_3 H(q), \quad (21)$$

where  $\phi$  and  $\lambda$  are the parameters for the traction predictor and the normalizing flow, and the weights  $w_1, w_2, w_3 \geq 0$  are hyperparameters. As simulation results suggest in Sec. V-C, the multi-objective loss (21) leads to more stable training and steadily improves performance given more empirical samples.

#### E. Network Architecture and Training

Semantic and elevation features of the terrain are encoded via convolutional kernels, and processed by two decoder heads for predicting the linear and angular traction distributions via transposed convolutions, before a soft-max layer that generates traction distributions in each terrain cell. The latent features from the bottleneck layer are passed to the normalizing flow to obtain density estimates. Because the bottleneck layer has a smaller spatial dimension than the original map, we use bilinear interpolation to provide density estimates for each terrain

<sup>1</sup>Taking cumulative sum and squared difference are convex operations.

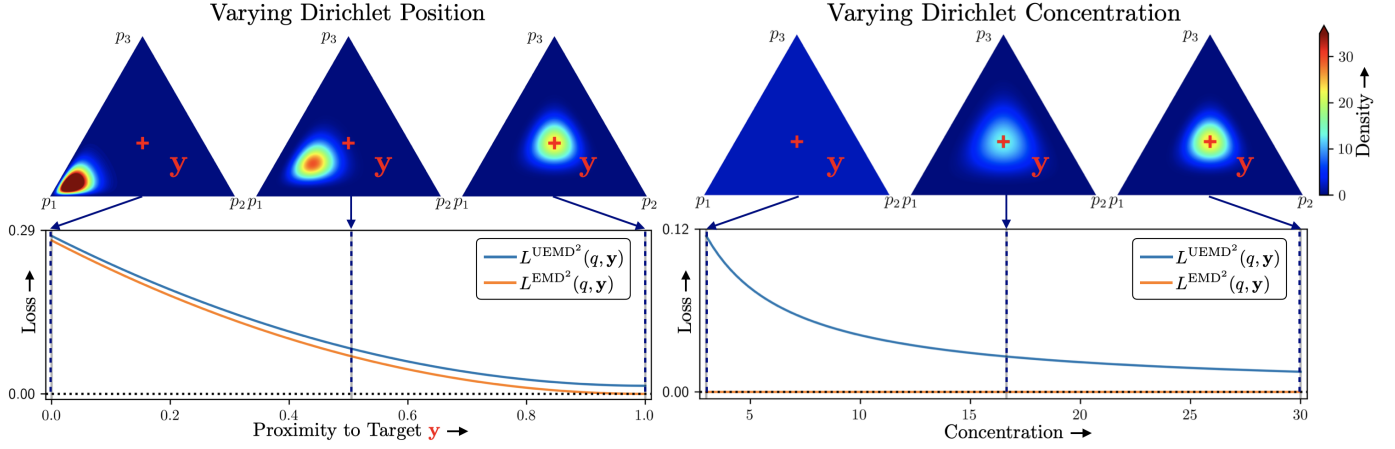


Fig. 5: Analyzing the difference between the standard  $\text{EMD}^2$  loss and our proposed  $\text{UEMD}^2$  loss on a toy example with three bins  $p_1, p_2, p_3$ . Each blue triangle represents a predicted Dirichlet distribution  $q$  visualized as a probability density over the 3-simplex; each point inside the simplex corresponds to a categorical distribution over the three bins. The red cross  $+$  denotes the location of the target label distribution  $y$  in the training set. A Dirichlet distribution can be parametrized by two quantities: the position of its mean and the concentration around its mean. **Left:** varying the position of the Dirichlet while keeping its concentration fixed. In this case, both losses behave similarly and as desired—they encourage the predicted Dirichlet to be close to the target label distribution. **Right:** varying the concentration of the Dirichlet while keeping its position fixed to the ground truth. Since  $\text{EMD}^2$  only depends on the position of the Dirichlet mean, it is constant with respect to varying concentration. However, our proposed  $\text{UEMD}^2$  encourages the predicted Dirichlet to have high concentration (low epistemic uncertainty). Learning to predict low epistemic uncertainty for in-distribution training examples is essential for calibrated uncertainty prediction and detecting out-of-distribution examples, as opposed to being indifferent to the concentration.

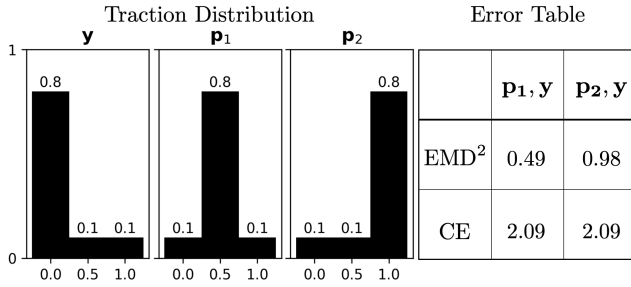


Fig. 6: Difference between  $\text{EMD}^2$  and CE. Given the ground truth  $y$  and the predictions  $p_1$  and  $p_2$ , CE produces the same values while  $\text{EMD}^2$  penalizes  $p_2$  more. In practice,  $\text{EMD}^2$  is more desirable because it accounts for the cross-bin relationship among the discretized traction values.

cell. We first compute the empirical linear and angular traction distributions from the training set by computing histograms for each cell (in the overhead map) that the robot traverses during data collection. During training, we weigh the loss for each cell by the number of measurements accumulated in the cell in order to discount rarely visited terrain.

We follow the two-step training procedure outlined in [1]. First, we jointly train the traction distribution predictor and the normalizing flow. After convergence, we freeze the encoder-decoder and only fine-tune the normalizing flow. This strategy improves OOD detection accuracy. However, we observe no improvement by performing “warm-up training” for the normalizing flow prescribed by [1].

#### IV. PLANNING WITH LEARNED TRACTION DISTRIBUTION

When the terrain features are novel and epistemic uncertainty is high, traction predictions may be unreliable and the robot should avoid this terrain. However, when epistemic uncertainty is low, we propose a risk-aware cost formulation that accounts for aleatoric uncertainty, allowing the robot to trade off the risk of immobilization (getting stuck) with potential time savings obtained from traversing terrain with

uncertain traction. The proposed cost formulation can be substituted in the nominal objective (4), that can then be optimized using any appropriate planning algorithm such as MPPI. To facilitate motion planning, the predicted traction distributions and normalized densities of latent features are stored in a map  $M$ . Each cell  $M^{h,w}$  indexed by row  $h$  and column  $w$  stores the expected traction PMF  $\mathbf{p}_{\mathbf{o}^{h,w}}^{\text{post}} \in \mathbb{R}_{\geq 0}^B$  (11) and the normalized density  $g_{\mathbf{o}^{h,w}} \in \mathbb{R}$  (10) predicted by the NN based on the associated terrain feature  $\mathbf{o}^{h,w}$  in that cell.

##### A. Conditional Value at Risk (CVaR)

We adopt the Conditional Value at Risk (CVaR) as a risk metric because it satisfies a group of axioms important for rational risk assessment [42]. The conventional definition of CVaR assumes the worst-case occurs at the right tail of the distribution. We define CVaR for a random variable  $Z$  at level  $\alpha \in (0, 1]$  for both the right and left tails of its distribution (see Fig. 7) as follows:

$$\text{CVaR}_{\alpha}^{\rightarrow}(Z) := \frac{1}{\alpha} \int_0^{\alpha} \text{VaR}_{\tau}^{\rightarrow}(Z) d\tau, \quad (22)$$

$$\text{CVaR}_{\alpha}^{\leftarrow}(Z) := \frac{1}{\alpha} \int_0^{\alpha} \text{VaR}_{\tau}^{\leftarrow}(Z) d\tau, \quad (23)$$

where the right and left Values at Risk (VaR) are defined as:

$$\text{VaR}_{\alpha}^{\rightarrow}(Z) := \min\{z \mid p(Z > z) \leq \alpha\}, \quad (24)$$

$$\text{VaR}_{\alpha}^{\leftarrow}(Z) := \max\{z \mid p(Z < z) \leq \alpha\}. \quad (25)$$

Intuitively,  $\text{CVaR}_{\alpha}^{\rightarrow}(Z)$  and  $\text{CVaR}_{\alpha}^{\leftarrow}(Z)$  capture the expected outcomes that fall in the right tail and left tail of the distribution, respectively, where each tail occupies  $\alpha$  portion of the total probability. Note that the right-tail definitions are suitable for costs to be minimized, and the left-tail definitions are suitable for low traction values. When  $\alpha = 1$ , either definition of CVaR is equivalent to the mean of the distribution  $\mathbb{E}[Z]$ .

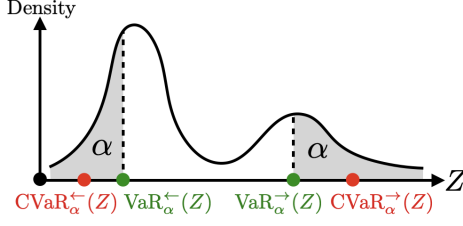


Fig. 7: This work defines two versions of Conditional Value at Risk (CVaR) to capture the worst-case expected values at either the left tail as  $\text{CVaR}_\alpha^-(Z)$  or the right tail as  $\text{CVaR}_\alpha^+(Z)$  for some random variable  $Z$ , where the worst-case scenarios constitute  $\alpha \in (0, 1]$  portion of total probability. The left-tail and right-tail Values at Risk (VaR) are defined as  $\text{VaR}_\alpha^-(Z)$  and  $\text{VaR}_\alpha^+(Z)$ .

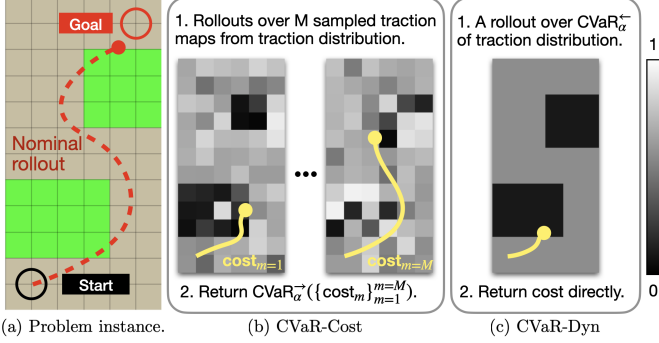


Fig. 8: Illustrations of CVaR-based costs in a toy problem with known traction distributions for regions of vegetation and dirt as shown in Fig. 11. Linear and angular traction models are assumed equal. (a) The state rollout based on nominal dynamics (i.e., no slip) does not account for uncertain traction. (b) CVaR-Cost [28] computes the expected costs in the right  $\alpha$ -quantile by evaluating the given control sequence over  $M$  traction map samples. (c) The proposed CVaR-Dyn requires only a single rollout over the traction map that contains the expected traction in the left  $\alpha$ -quantile.

### B. Risk-Aware Cost Formulations

To account for the risk due to the uncertain traction  $\psi_t$ , we first present an existing approach [28] that optimizes for the right-tail CVaR of the planning objective (CVaR-Cost), and propose a more computationally efficient method that accounts for the left-tail CVaR of traction (CVaR-Dyn). Visualizations for these two approaches can be found in Fig. 8.

1) *Worst-Case Expected Cost (CVaR-Cost [28])*: Given the control sequence  $\mathbf{u}_{0:T-1}$ , we want to approximate the worst-case expected value of the nominal objective  $C$  (4) due to uncertain terrain traction via sampling. First, we sample  $M > 0$  traction maps that each contains traction values sampled from the traction distribution  $\text{Cat}(\mathbf{p}_{\mathbf{o}_{h,w}}^{\text{post}})$  precomputed using NN and stored in every map cell indexed by height  $h$  and width  $w$ . Next, we compute the right-tail CVaR of the objective numerically using samples of the objective  $C$  obtained by evaluating the performance of  $\mathbf{u}_{0:T-1}$  over  $M$  traction maps:

$$c^{\text{CVaR-Cost}} := \text{CVaR}_\alpha^+(\{C(\mathbf{x}_{0:T}^m)\}_{m=1}^M), \quad (26)$$

where the  $m$ -th state rollout  $\mathbf{x}_{0:T}^m$  follows

$$\mathbf{x}_{t+1}^m = F(\mathbf{x}_t^m, \mathbf{u}_t, \psi_t^m), \quad \mathbf{x}_0^m = \mathbf{x}_0, \quad (27)$$

for  $t \in \{0, \dots, T-1\}$ . The traction parameter  $\psi_t^m$  is queried in the  $m$ -th sampled traction map based on state  $\mathbf{x}_t^m$ . Note that (26) can directly replace the nominal objective (4) and use MPPI to solve for the optimal control sequence. While sampled traction maps can be reused for evaluating different control sequences, the computation can still grow prohibitively

as the map size grows. Therefore, we propose a cheaper cost design that accounts for the left-tail CVaR of terrain traction.

2) *Worst-Case Expected Terrain Traction (CVaR-Dyn)*: Given the control sequence  $\mathbf{u}_{0:T-1}$ , we evaluate the nominal objective  $C$  (4) based on the state rollout simulated with the worst-case expected traction in the dynamical model, i.e.,

$$c^{\text{CVaR-Dyn}} := C(\bar{\mathbf{x}}_{0:T}), \quad (28)$$

where the state rollout follows

$$\bar{\mathbf{x}}_{t+1} = F(\bar{\mathbf{x}}_t, \mathbf{u}_t, \bar{\psi}_t), \quad \bar{\mathbf{x}}_0 = \mathbf{x}_0, \quad (29)$$

for  $t \in \{0, \dots, T-1\}$  and the worst-case expected traction  $\bar{\psi}_t$  is computed based on the corresponding traction distribution at some row  $h$  and height  $w$  determined by state  $\bar{\mathbf{x}}_t$ :

$$\bar{\psi}_t = \begin{bmatrix} \text{CVaR}_\alpha^-(\Psi_1) \\ \text{CVaR}_\alpha^-(\Psi_2) \end{bmatrix}, \quad \begin{bmatrix} \Psi_1 \\ \Psi_2 \end{bmatrix} \sim \text{Cat}(\mathbf{p}_{\mathbf{o}_{h,w}}^{\text{post}}), \quad (30)$$

where  $\mathbf{p}_{\mathbf{o}_{h,w}}^{\text{post}}$  (11) is precomputed using NN. Note that the proposed cost (28) can directly replace the nominal objective (4) and use MPPI to solve for the optimal control sequence. When  $\alpha = 1$ , the expected values of the traction parameters are used, equivalent to the approach in [27]. However, as the results in Sec. VI-B show for a go-to-goal task, planning with the worst-case expected traction can improve navigation performance when the traction distribution is not Gaussian.

*Remark 2.* Both (26) and the proposed (28) provide intuitive notions of risk that depend on the worst-case expected cost and terrain traction. Moreover, they are simple to tune with a single risk parameter  $\alpha$ , avoiding the need to manually design weights for a potentially large variety of terrain types.

*Remark 3.* While adding auxiliary penalties for trajectories entering low-traction terrain can generate similar risk-aware behaviors achievable by our approach, we show that using the proposed CVaR-Dyn (28) leads to solutions with better trade-offs between success rate and time-to-goal than ones achieved by using the nominal objective augmented with terrain penalties (see Fig. 13), while achieving higher success rate than CVaR-Cost (26) with less computation. In practice, using the proposed cost with auxiliary penalties for undesirable terrain types, such as OOD terrain, can lead to better performance (see Sec. VIII and Sec. IX-B).

## V. EVALUATION OF TRAVERSABILITY LEARNING PIPELINE

The proposed evidential traversability learning method is benchmarked using a synthetic terrain dataset (Sec. V-A) designed to simulate data scarcity during real-world data collection and provide ground truth traction distributions and OOD terrain masks. Several variants of the proposed loss (21) are compared based on prediction accuracy and OOD detection performance (Sec. V-C). To highlight the benefits of joint training and our UEMD<sup>2</sup> loss (20), we provide an ablation study in Sec. V-D. After analyzing the proposed planner in Sec. VI, Sec. VII contains key results that show improved navigation performance due to our proposed loss.

As comparing uncertainty quantification methods is not the main focus of this work, we refer interested readers to [1] that has demonstrated the computational advantages,



learning accuracy and OOD detection performance of the NN architecture used in this work compared to the other state-of-the-art uncertainty quantification methods.

### A. Synthetic 3D Terrain Datasets

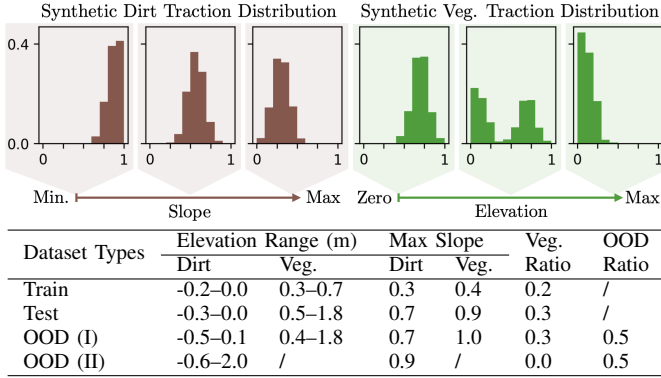


TABLE I: Synthetic terrain dataset for benchmarking loss functions. The ground truth traction distributions for dirt are unimodal Gaussian distributions whose mean increases with terrain slope that indicates roughness of the terrain. Traction distributions for vegetation are based on elevation, where the traction is bi-modal for intermediate elevation and uni-modal at the minimum and maximum elevations. Note that OOD dataset (I) consists of mixed terrain types, but OOD (II) contains no vegetation to ensure that learned models do not rely solely on semantics for OOD detection.

The synthetic dataset contains randomly generated 3D terrain with ground truth traction distributions generated based on geometric properties (elevation and slope) and semantic types (dirt and vegetation); details are available in Table I. Note that terrain slopes are only used for generating the ground truth traction distributions, but are not used as inputs to the NN. For simplicity, we use the same traction distribution for both linear and angular components, and dependencies only exist between dirt and terrain slope, and vegetation and terrain elevation. While more complex traction distributions can be designed, our dataset is sufficient for supporting our contributions. In total, there are 5 training, 20 test, and 40 OOD environments that are 30 meters in width and height, 0.5 meters in resolution, as well as different elevations slopes and vegetation ratios, where the training dataset is intentionally small in order to examine the generalization of learned models. Every training environment is split into equal parts for training and cross validation respectively. The synthetic environments are selectively visualized in Fig. 9. To simulate real-world data collection, traction samples are only obtained along a circular path. Moreover, we consider the impact of increasing the number of samples by multiplying the base measurement counts by factors  $10^k$  where  $k \in \{0, \dots, 4\}$ . The test environments are used for both measuring the prediction accuracy and analyzing the navigation performance using learned models (see Sec. VII). The OOD environments are available with binary masks for terrain cells with unseen terrain properties, based on slope and elevation in the training dataset. This dataset can be used to benchmark OOD detection performance.

### B. Model Training

We use the same network architecture for all the loss functions, where the traction predictor consists of a convo-

lutional encoder and a transposed convolutional decoder to produce traction distribution with a softmax output layer for the entire feature map. The latent space features are passed to a radial flow [55] and we use a constant certainty budget that scales exponentially with the latent dimension for numerical purposes [1]. As discussed in Sec. III-E, we perform fine-tuning of the flow while freezing the main body after the joint training loss has converged. Hyperparameter sweeps are conducted over learning rates in  $[1e-4, 3e-4, 1e-3]$  for the Adam optimizer, and entropy weights in  $[0, 1e-6, 1e-5]$  when UEMD<sup>2</sup> and UCE are used separately. For the weighted sum of UEMD<sup>2</sup> and UCE, we fix the UCE term and consider additional weights for UEMD<sup>2</sup> in  $[0.1, 1, 10]$ . For each combination of hyperparameters, we train the model with five random seeds and select the best model based on validation EMD<sup>2</sup> error averaged over the seeds because empirically, we have found that selecting models based on validation EMD<sup>2</sup> instead of Kullback-Leibler (KL) divergence leads to improved performance for *all* models. To guarantee fairness for the state-of-the-art and not clutter the figures, we only present the results for models selected based on validation KL divergence for the UCE loss.

### C. Prediction Accuracy and OOD Detection Performance

The comparison among variations of the proposed loss (21) is presented in Fig. 10, where the prediction accuracy is measured by EMD<sup>2</sup> and KL divergence, and the accuracy of OOD detection using the density for latent features is measured by area under the receiver operating characteristic curve (AUC-ROC) and area under the precision-recall curve (AUC-PR). Note that AUC-ROC and AUC-PR are standard metrics for binary classification that are invariant to scale and offset. Intuitively, a score of 0.5 means the classifier is as good as random guesses, and a score of 1 indicates a perfect classifier. To show the best performance achievable by the state-of-the-art with unlimited traction samples during training, we include models trained with UCE using the *ground truth traction distributions* in the training environments.

The main takeaway from the benchmark is that the models trained with the proposed weighted sum of UEMD<sup>2</sup> and UCE achieves the best prediction accuracy in *both* EMD<sup>2</sup> and KL divergence. Furthermore, the weighted-sum objective regularizes the traction predictor’s latent space better, leading to more stable improvements in test performance in both prediction accuracy and OOD detection as training samples become more abundant. In contrast, the other loss designs are more prone to overfitting, which worsens prediction accuracy when given less noisy empirical traction distributions estimated based on more empirical samples. Notably, compared to EMD<sup>2</sup>-based losses, UCE does not capture the cross-bin relationship of the traction distribution, which leads to worse regularized latent space that causes unstable OOD detection performance (even for UCE trained with ground truth traction distributions in the training environments). While UEMD<sup>2</sup> results in higher KL error than UCE in general, Fig. 14 shows that training with EMD<sup>2</sup>-based losses leads to better navigation performance when data is scarce, which is attractive for real-world applications where data collection is expensive.

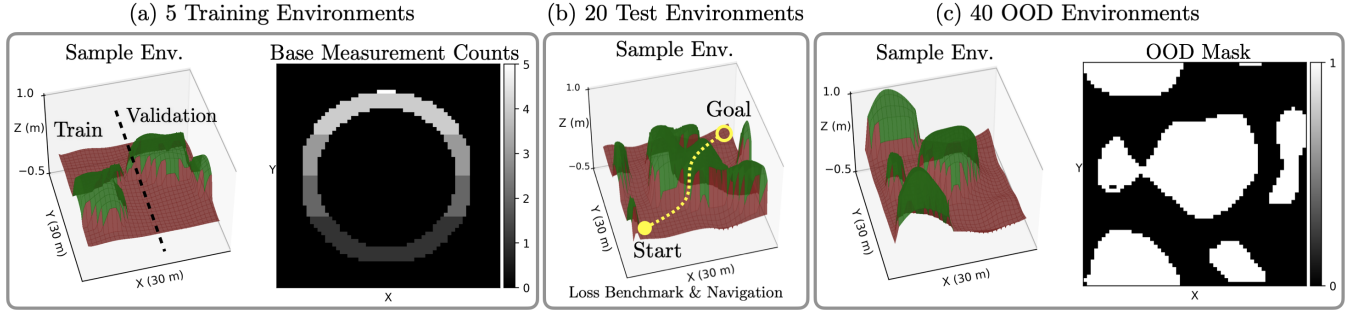


Fig. 9: The synthetic 3D terrain dataset with dirt (brown) and vegetation (green) semantic types. (a) In each training environment, there are limited traction measurements along a pre-specified circular path to mimic real-world data collection where a robot can only cover a limited area and collect a finite number of measurements. Each environment is split into two for cross validation when choosing hyperparameters. Furthermore, we analyze the effect of a varying number of measurements by multiplying the base measurement counts (see Fig. 10). (b) The test environments contain novel terrain features for analyzing the traction prediction accuracy. To support the key argument that  $\text{EMD}^2$  is a better indicator for navigation performance, models trained with different loss functions are deployed in the test environments for go-to-goal tasks (see Sec. VII). (c) Compared to the test environments, the OOD dataset additionally provides binary masks for the novel terrain with elevation and/or slope not observed during training.

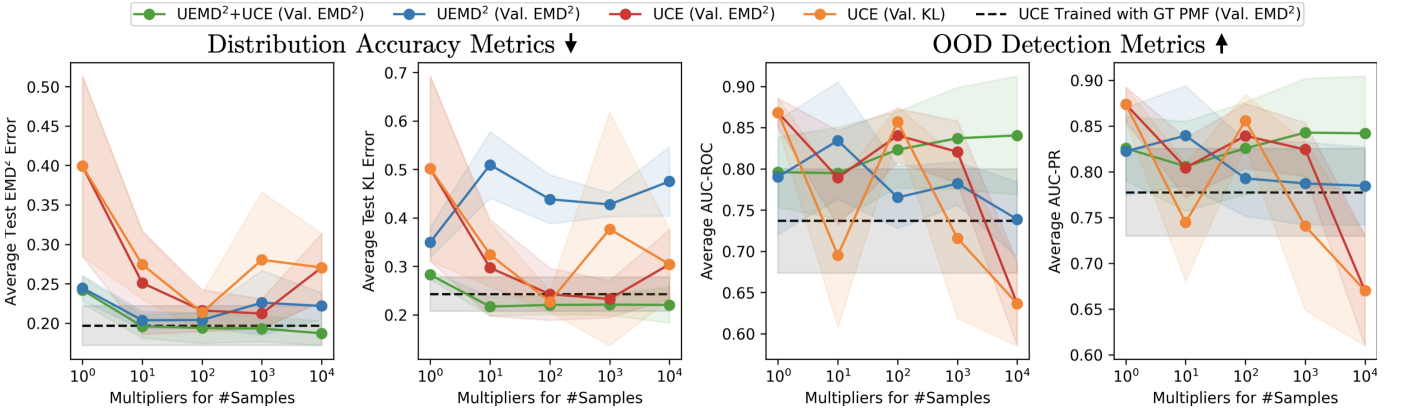


Fig. 10: Prediction errors measured in  $\text{EMD}^2$  and KL divergence (the lower, the better), and OOD detection accuracy measured in AUC-ROC and AUC-PR (the higher, the better). The legend for each loss function is followed in parentheses with the selection criteria used for choosing hyperparameters. The results show the average values and the standard deviations across random seeds. Overall, the proposed weighted sum of  $\text{UEMD}^2$  and UCE leads to the best prediction accuracy and steadily improving OOD detection performance as more samples become available. In contrast, as more samples lead to better estimated empirical traction distributions, the prediction accuracy achieved by the other loss designs eventually degrades due to overfitting. In addition, compared to  $\text{EMD}^2$ -based losses, UCE is worse at capturing the cross-bin relationship among the discrete traction values, which leads to poorly regularized latent space that causes unstable OOD detection performance, even when trained with the ground truth traction distributions in the training environments.

#### D. Ablation Study for $\text{UEMD}^2$ and Joint Training

While the benefits of using uncertainty-aware loss and joint training have been established in [1] for UCE, we present a similar ablation study for  $\text{UEMD}^2$  for completeness in Table. II. We set the sample multiplier to 10 for simplicity, but similar conclusions can be drawn with more samples. The takeaway is that both joint training and uncertainty awareness are required to achieve improved accuracy in  $\text{EMD}^2$  and OOD detection. Despite these improvements, the results in Fig. 10 show that both  $\text{UEMD}^2$  and UCE are required to achieve more consistent and steadily improving performance in prediction accuracy and OOD detection performance.

TABLE II: Ablation study for  $\text{UEMD}^2$  and joint training.

Loss	Test $\text{EMD}^2$ ↓	AUC-ROC ↑	AUC-PR ↑
$\text{UEMD}^2$ (Joint)	$0.204 \pm 0.01$	$0.834 \pm 0.07$	$0.840 \pm 0.05$
$\text{EMD}^2$ (Joint)	$0.236 \pm 0.02$	$0.802 \pm 0.04$	$0.830 \pm 0.03$
$\text{EMD}^2$ (Disjoint)	$0.228 \pm 0.03$	$0.665 \pm 0.14$	$0.770 \pm 0.07$

## VI. EVALUATION OF RISK-AWARE PLANNERS

Using simulated 2D semantic environments, we show that the proposed CVaR-Dyn outperforms existing approaches [20],

[27] that assume the nominal traction or the expected traction, while achieving similar performance with CVaR-Cost [28] when having low risk tolerances. Moreover, we discuss the advantages and limitations of CVaR-Dyn compared to the approach that assumes nominal traction while penalizing trajectories moving through terrain with high aleatoric uncertainty. For simplicity, we consider a grid world where dirt and vegetation cells have known traction distributions, as shown in Fig. 11. Vegetation patches are randomly spawned with increasing probabilities at the center of the arena, and a robot may experience a significant slow-down for certain vegetation cells due to vegetation’s bi-modal traction distribution. The mission is deemed successful if the goal is reached within 15 s to prevent simulations from running indefinitely if the robot encounters near-zero traction.

#### A. Planner Implementation

We adopt MPPI [3, Algorithm 2] because it is derivative-free and parallelizable on GPU. The planners run in a receding horizon fashion with 100 timesteps at 0.1 s intervals. The maximum linear and angular speeds are 3 m/s and  $\pi$  rad/s, and the noise standard deviations for the control signals are

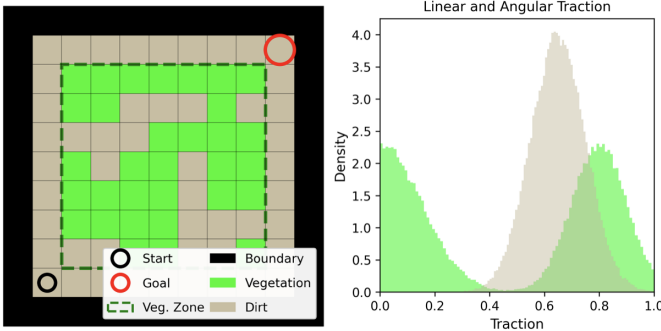


Fig. 11: The simulation environment where a robot has to move from start to goal as fast as possible within the bounded arena. Linear and angular traction parameters share the same distribution for simplicity. Vegetation terrain patches are randomly sampled at the center in the vegetation zone.

2 m/s and 2 rad/s. The number of control rollouts is 1024, and the number of sampled traction maps is 1024 (only for CVaR-Cost). We use PMFs with 20 uniform bins to approximate the traction distribution. A computer with Intel Core i9 CPU and Nvidia GeForce RTX 3070 GPU is used for the simulations, where the majority of the computation happens on the GPU. The CVaR-Cost planner is the most expensive to compute, but it is able to re-plan at 15 Hz while sampling new control actions and maps with dimensions of  $200 \times 200$ . Planners that do not sample traction maps can be executed at over 50 Hz.

### B. Navigation Performance

The benchmark results can be found in Fig. 12, where we compare the proposed CVaR-Dyn against CVaR-Cost [28], WayFAST [27] that uses the expected traction and the technique in [20] that assumes the nominal traction while adjusting the time cost with the CVaR of linear traction. Overall, we sample 40 different semantic maps and 5 random realizations of traction parameters for every semantic map. The traction parameters are drawn before starting each trial and remain fixed. The takeaway is that the proposed CVaR-Dyn achieves better or similar success rate than the other methods when the risk tolerance  $\alpha$  is sufficiently low.

To compare CVaR-based methods against the method that plans with the nominal objective with auxiliary penalties for vegetation terrain with high aleatoric uncertainty, we focus on the most challenging setting with 70% vegetation, where it is easy to get stuck in local minima. The benchmark result is shown in Fig. 13, where we compare the trade-offs between success rate and time-to-goal achieved by different methods. First, note that CVaR-Cost suffers from low success rate due to conservativeness, whereas the proposed CVaR-Dyn achieves higher success rates when  $\alpha$  is low. WayFAST [27] also suffers from low success rate, because planning with the expected traction does not capture the risk in noisy terrain traction. Although CVaR-Dyn achieves better trade-offs than having vegetation penalties, its conservativeness in considering the CVaR of traction prevents it from achieving 100% success rates. Therefore, when domain knowledge is available, auxiliary costs can be used together with CVaR-Dyn to achieve a higher success rate desirable in practice, but cost tuning may be challenging given a large variety of terrain types.

## VII. OPTIMIZING FOR $\text{EMD}^2$ IMPROVES NAVIGATION

To support the key argument that  $\text{EMD}^2$  is a better metric than KL divergence for measuring the quality of learned traction distributions for navigation, we evaluate the navigation performances when using models trained with different losses presented in Sec. V. The models are deployed in the same test environments visualized in Fig. 9, where each map is 30 m in width and height and the start and goal positions are at the opposite diagonal corners. To not clutter the results, we only focus on the proposed CVaR-Dyn planner with  $\alpha = 0.4$  and the same MPPI setup in Sec. VI-A, but similar trend can be observed with different choices of  $\alpha$ . Consistent with the loss benchmark in Sec. V, each loss is trained with 5 random seeds and 5 levels of data abundance. For each of the 20 test maps, we consider 5 randomly sampled traction maps and run the mission 3 times. The final results averaged over training seeds can be found in Fig. 14, where all trials are successful within reasonable time, so the success rate is omitted.

Importantly, when the amount of data is low,  $\text{UEMD}^2$  outperforms UCE in time-to-goal even though  $\text{UEMD}^2$  leads to worse KL error than UCE loss as shown in Fig. 10. This validates our intuition that  $\text{EMD}^2$  captures the cross-bin information of discretized traction values better, which facilitates the learning of traction distribution in low-data regime and leads to better navigation performance. However, as more data becomes available and the empirical traction distributions become better estimated, the performance of the proposed weighted sum of  $\text{UEMD}^2$  and UCE steadily improves and outperforms  $\text{UEMD}^2$  whose performance suffers from over-fitting as discussed in Sec. V. Furthermore, the navigation performance of the proposed hybrid loss approaches the best possible performance of the state-of-the-art UCE loss when trained on ground truth traction distributions in the training environments, indicating good generalization of our approach using only limited data. For reference, the figure also provides the lower bound for the navigation performance based on the ground truth traction models in the test environments.

## VIII. BENEFITS OF AVOIDING OOD TERRAIN

We demonstrate the benefit of the proposed density-based confidence score (10) for detecting terrain with high episodic uncertainty. To simulate training and test environments, we leverage the data collected in two distinct forests using Clearpath Husky, where the first one (visualized in Fig. 4) is used for training, and the second one (whose semantic top-down view is shown in Fig. 15) is used as the test environment. The environment models were built using semantic octomaps [52] that fused lidar points and segmented RGB images based on the 24 semantic categories in the RUGD dataset [54]. The traction values will be drawn from the test environment's empirical traction distributions learned by a separate NN as the proxy ground truth. We use the proposed CVaR-Dyn with a low risk tolerance  $\alpha = 0.2$  to handle the noisy terrain traction. Two specific start-goal pairs have been selected to highlight the most challenging parts of the test environment with novel features. Each start-goal pair is repeated 10 times for each selected confidence threshold

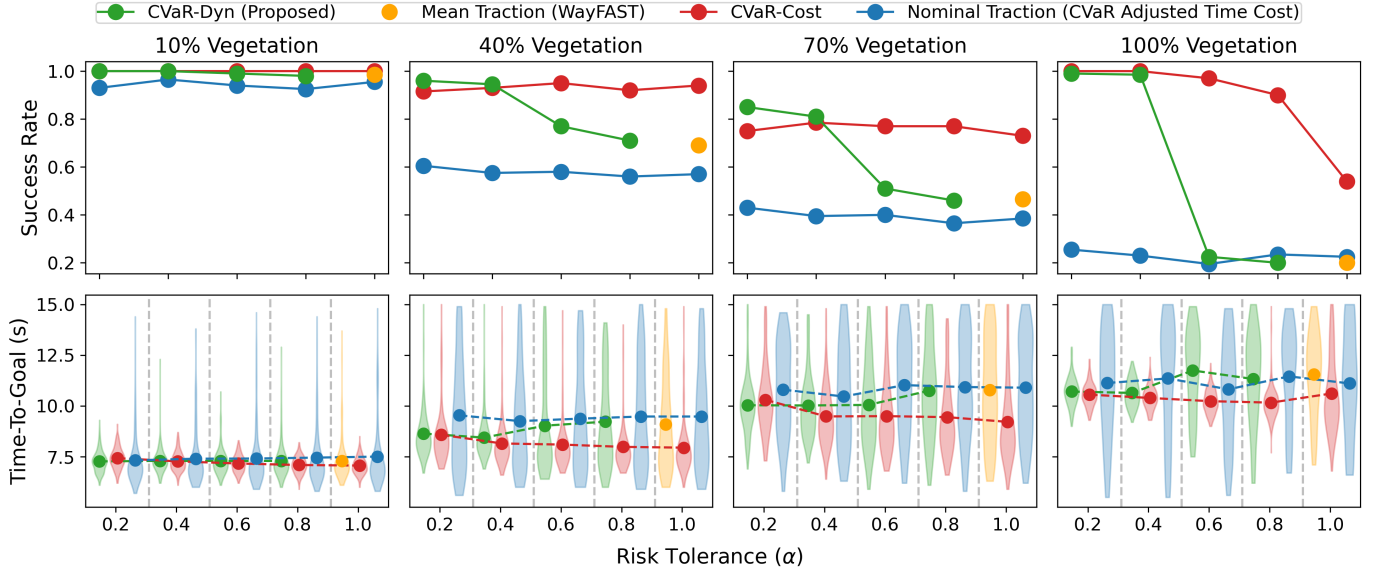


Fig. 12: Results comparing the proposed method CVaR-Dyn (28) against CVaR-Cost (26) and the existing methods based on the expected traction (WayFAST [27]) or the nominal traction [20] (i.e., no slip). Note that a mission is successful if the goal is reached within 15 s. Overall, when the risk tolerance is sufficiently low (e.g.,  $\alpha = 0.2$ ), CVaR-Dyn achieves similar or better success rate and time-to-goal compared to the CVaR-Cost planner and outperforms both WayFAST and the method that assume nominal traction. While it is possible for CVaR-Cost to achieve really low time-to-goal, it suffers from low success rate which is undesirable in practice.

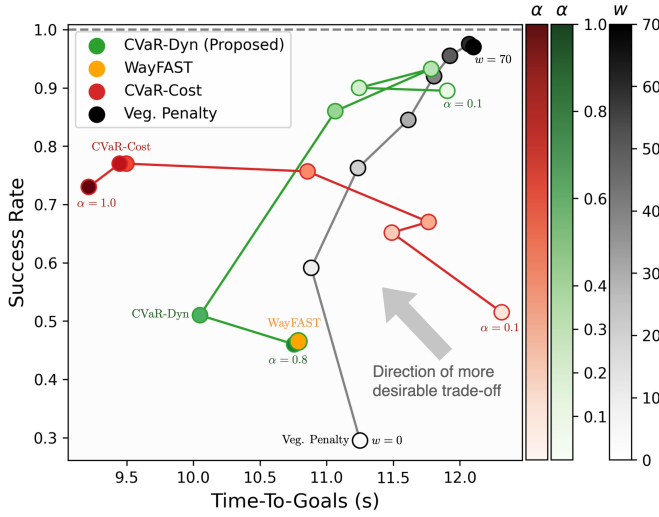


Fig. 13: In the most challenging scenario of 70% vegetation, solutions obtained by CVaR-Dyn when  $\alpha < 1$  (green) achieve a better trade-off between success rate and time-to-goal than ones achieved by WayFAST (CVaR-Dyn with  $\alpha = 1$ ) and the baseline that adds auxiliary penalty  $w > 0$  for states entering vegetation terrain (black) by being in the upper left of the figure. Although the CVaR-Cost planner (red) achieves the best time-to-goal with high  $\alpha$ , its performance suffers significantly from the conservativeness of using CVaR of the objective, which leads to worsening success rate and time-to-goal as  $\alpha$  lowers. Note that the success rate of CVaR-Dyn plateaus as  $\alpha$  decreases due to shorter state rollouts that lead to local minima. The conservativeness of the proposed CVaR-Dyn planner can be mitigated by adding auxiliary penalties for undesirable terrain to improve navigation performance when domain knowledge is available (see Sec. VIII).

$g^{\text{thres}}$ . We investigate two ways to prevent the planner from entering terrain that is classified as OOD (10) by either 1) assigning zero traction, or 2) adding large penalties. The mission is deemed successful if each goal is reached within 30 s, because many locations have zero traction that traps the robot indefinitely.

As shown in Fig. 16, the success rate improves by up

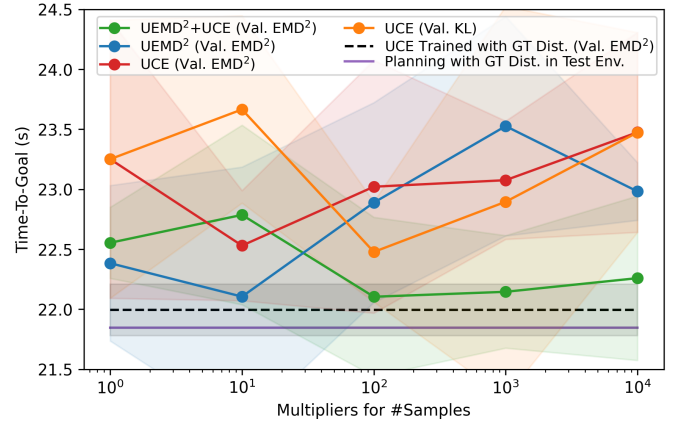


Fig. 14: Navigation performance using learned traction models trained with different loss designs in the test environments shown in Fig. 9. The results show the average values and the standard deviations across random seeds used during training. Even though UEMD<sup>2</sup> leads to worse KL divergence as shown in Fig. 10, it still outperforms UCE in achieving faster navigation in the low-data regime. Overall, the proposed weighted sum of UEMD<sup>2</sup> and UCE leads to steadily improving performance as more samples become available, but using UEMD<sup>2</sup> or UCE alone leads to less stable performance due to overfitting discussed in Sec. V. Note that the navigation performance of the proposed hybrid loss approaches the best possible navigation performance using the ground truth (GT) traction models in the test environments and the best possible navigation performance of the state-of-the-art UCE loss trained with the GT traction distributions in the training environments.

to 30% as  $g^{\text{thres}}$  increases, because the robot avoids regions with unreliable traction predictions. Interestingly, using CVaR-Dyn with soft penalties for OOD terrain leads to better time-to-goal while retaining a similar success rate, because the auxiliary costs for OOD terrain make it easier for the planner to find trajectories that avoid the OOD terrain. Therefore, it is advantageous to use CVaR-Dyn with auxiliary costs when domain knowledge is available to achieve both a high success rate and fast navigation in practice.



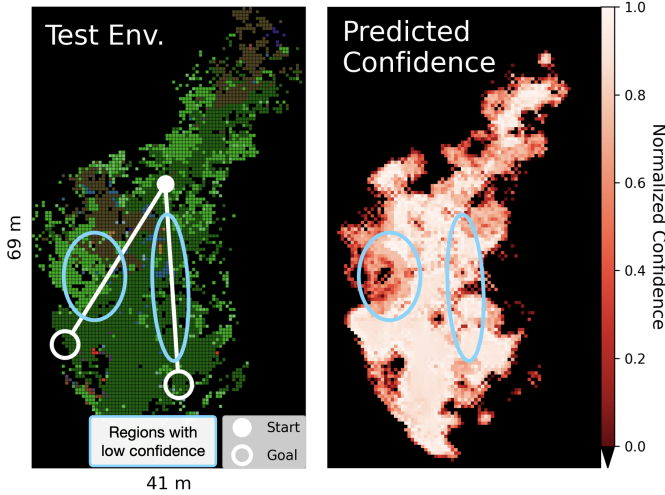


Fig. 15: (Left) In the test environment, the simulated robot has to reach two goals selected to highlight the danger of using unreliable network predictions. (Right) The latent density-based confidence score (10) indicates the amount of epistemic uncertainty for the predicted traction distribution, where unknown terrain and known terrain with negative scores are shown in black. Note that the brown semantic region (mulch) at the top has confidence below zero due to the presence of unknown cells, in contrast to the brown semantic region to the left with much fewer unknown cells.

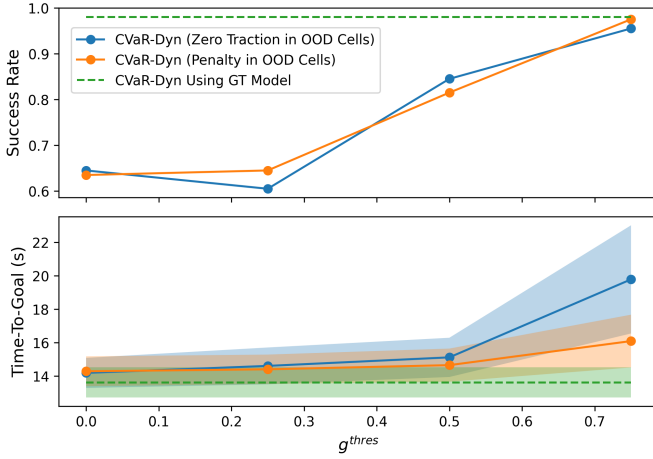


Fig. 16: Navigation success rate improves by avoiding OOD terrain when deploying a trained NN in a novel environment. The results show the average values and the standard deviations. We select CVaR-Dyn with  $\alpha = 0.2$  and  $g^{\text{thres}} = 0$  as the planner, but similar conclusions can be drawn using a different planner. The OOD terrain is handled by either assigning zero traction (blue) or imposing penalties (orange). The performance of the planner that uses the ground truth (GT) traction is also shown to demonstrate the best performance. Overall, higher  $g^{\text{thres}}$  improves the success rate at the cost of higher time-to-goal, because there are more OOD terrain cells to avoid. However, auxiliary penalties for OOD terrain make it easier for the planner to find solutions that lead to the goal. Notably, the average success rate when  $g^{\text{thres}} = 0.75$  approaches 1, indicating that the learned traction model generalizes well to terrain with high confidence values in the test environment.

## IX. HARDWARE EXPERIMENTS

To evaluate the effectiveness and feasibility of the proposed approach in practice, we designed two experiment scenarios—an indoor race track scenario with fake vegetation using an RC car (Sec. IX-A) and a more challenging outdoor scenario using a legged robot (Sec. IX-B). While both scenarios show that the proposed CVaR-Dyn planner leads to the best navigation performance, the outdoor scenario also shows the benefits of avoiding OOD terrain. In practice, the control signals gener-

ated by MPPI are very noisy, so we plan in the derivative space of the nominal control [56] to generate smooth trajectories.

### A. Indoor Racing with an RC Car

An overview of the indoor setup is provided in Fig. 17, which shows the 9.6 m by 8 m arena populated with turf and fake trees used to mimic outdoor vegetation. The 0.33 m by 0.25 m RC car was equipped with a RealSense D455 depth camera, an Intel Core i7 CPU, and a Nvidia RTX 2060 GPU. The robot ran onboard traction prediction, motion planning, and online elevation mapping with 0.1 m resolution, but Vicon was used for ground truth pose and velocity estimation. We identified vegetation by extracting the green image pixels instead of using a standalone NN semantic classifier in order to conserve GPU resources. The bicycle model (3) was used for this experiment, and the traction values were obtained by analyzing the commanded linear velocities, steering angles, and the ground truth velocities from Vicon. The traction model was trained based on 10 min of driving data with the proposed loss function (21), where UEMD<sup>2</sup> and UCE were both weighted by 1 and the entropy term was weighted by  $1e-5$  based on empirical tuning. The learned traction distributions are visualized in Fig. 17a to highlight multimodality. At deployment time, the robot ran 2 laps around the race track along the ellipsoidal reference path, while deciding between a shorter path covered with vegetation or a less risky detour, as shown in Fig. 17b. We designed a moving goal region along the reference path, called the “carrot goal”, that maintained a constant 75 degree offset from the robot’s projected position on the ellipsoidal reference path. In addition to CVaR-Cost and the proposed CVaR-Dyn, we considered an intelligent baseline that assumes nominal traction but assigns auxiliary penalties for low-lying vegetation between 5 cm and 15 cm that could cause unfavorable driving conditions. All methods avoided the trees via auxiliary penalties. All planners considered 1024 rollouts while planning at 20 Hz with 5 s look-ahead. Due to computational constraints, CVaR-Cost only considered 400 traction map samples. We set the maximum linear speed and steering angle to be 1.5 m/s and 30 degrees.

The final outcomes are summarized in Fig. 19, where we considered 3 risk tolerances for each method and repeated the race 5 times. Qualitative visualizations are provided in Fig. 18 to show the failure cases of each method. Overall, CVaR-Dyn with  $\alpha = 0.8$  achieved the best time-to-goal and success rate. In comparison, the baseline and the CVaR-Dyn planner with  $\alpha = 1$  (WayFAST [27]) both suffered from noisy real-world traction, causing wide turns. The CVaR-Cost planner was the most conservative by frequently taking the detour, and its performance suffered from the reduced number of traction map samples due to computational constraints. Note that the results are consistent with Fig. 12 in that there exists a risk tolerance that enables CVaR-Dyn to outperform CVaR-Cost in terms of both time-to-goal and success rate, and, consistent with Fig. 13, that CVaR-Dyn achieves better time-to-goal than the baseline while maintaining a higher success rate. In summary, these results suggest that CVaR-Dyn is an attractive choice for real-world applications because it directly accounts for the

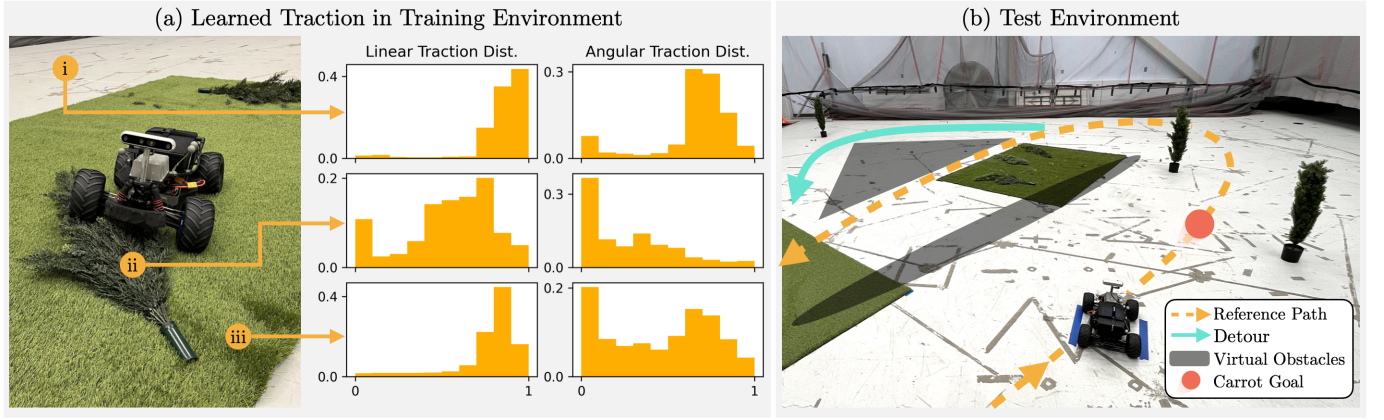


Fig. 17: The training and test environments used for the indoor racing experiments. (a) The training environment consisted of a single turf with two fallen trees for simulating bushes. Learned linear and angular traction distributions are visualized for selected regions with (i) hard floor, (ii) fallen tree, and (iii) turf. Note that the bi-modality of traction distribution over the vegetation could cause the robot to slow down significantly. (b) The test environment contained two turfs, three fallen trees, three standing trees, and virtual obstacles. The robot was tasked to drive two laps following a carrot goal along the reference path while deciding between a detour without vegetation and a shorter path with vegetation.

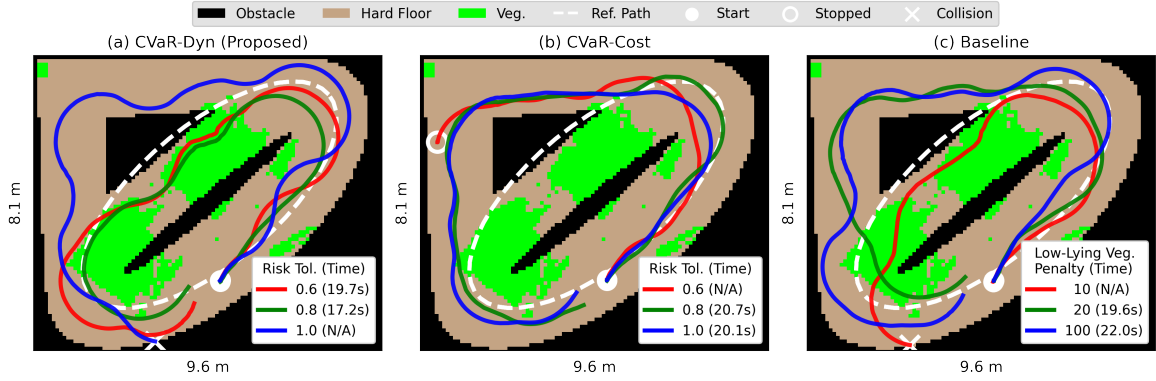


Fig. 18: Representative trials of the indoor experiments for highlighting the failure modes of the planners. We only show the first lap out of the two laps for clarity. (a) As  $\alpha$  decreased, the proposed CVaR-Dyn preemptively turned early to enter the shortcut paths, whereas WayFAST (CVaR-Dyn with  $\alpha = 1$ ) did not account for the risk of under-steering, so it always turned too late for the shortcut. (b) CVaR-Cost was the most conservative by only taking the detour and sometimes coming to a stop near obstacles. (c) When the soft penalty was low, the baseline was more risk-tolerant and chose to take the shortcut, but the experienced traction differed significantly from the nominal traction, which caused more collisions. As the soft penalty increased, the planner became more conservative and took the detours, but planning with nominal traction led to significant under-steering that limited the navigation performance.

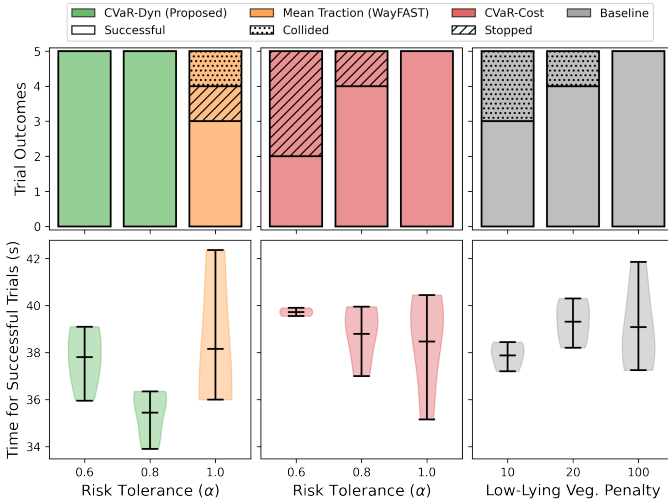


Fig. 19: Outcomes and mission time (5 trials) for the indoor experiments. Overall, the proposed CVaR-Dyn with  $\alpha = 0.8$  achieved the best performance. CVaR-Cost suffered from conservativeness and had to issue 0 velocity commands to stop the robot before hitting obstacles. By planning with the nominal traction or the expected traction, the baseline and WayFAST (CVaR-Dyn with  $\alpha = 1$ ) led to worse time-to-goal and a higher chance of collision.

risk of obtaining low traction in the control rollouts without incurring extra computation (like CVaR-Cost) or requiring human expertise in designing semantics-based costs.

### B. Outdoor Navigation with a Legged Robot

The outdoor experiments were designed to test the effectiveness and feasibility of the proposed local planners, show the benefits of avoiding OOD terrain, as well as the applicability of our methods on a legged robot. An overview of the outdoor setup is shown in Fig. 20. A Boston Dynamics Spot robot was fitted with a RealSense D455, an Ouster OS0 lidar, and an Nvidia Jetson AGX Orin with good power efficiency but less powerful computation than the computers used in previous experiments. The unicycle model (2) was used for this experiment, and traction values were obtained by comparing the commanded velocities and Spot's built-in odometry. The environment model was built using a semantic octomap [52] that fused lidar points and segmented RGB images based on the 24 semantic categories in the RUGD dataset [54]. The traction model was trained based on 5 minutes of walking data with the proposed loss function (21) with the same weights used for the indoor experiment. The learned traction

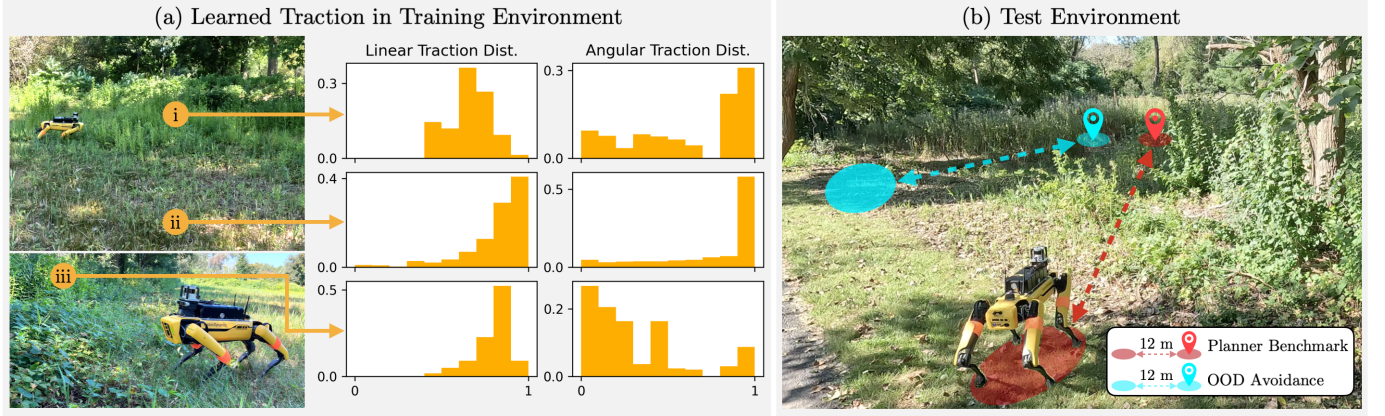


Fig. 20: The outdoor training and test environments with a legged robot. (a) The outdoor environment consisted of vegetation terrain with different heights and densities. Predicted linear and angular traction distributions are visualized for selected regions with (i) tall grass, (ii) short grass, and (iii) dense bushes. Unlike wheeled robots, a legged robot typically has good linear traction through vegetation, but angular traction may exhibit multi-modality due to the greater difficulty of turning. (b) Two start-goal pairs were used to benchmark the planners and analyze the benefits of avoiding OOD terrain.

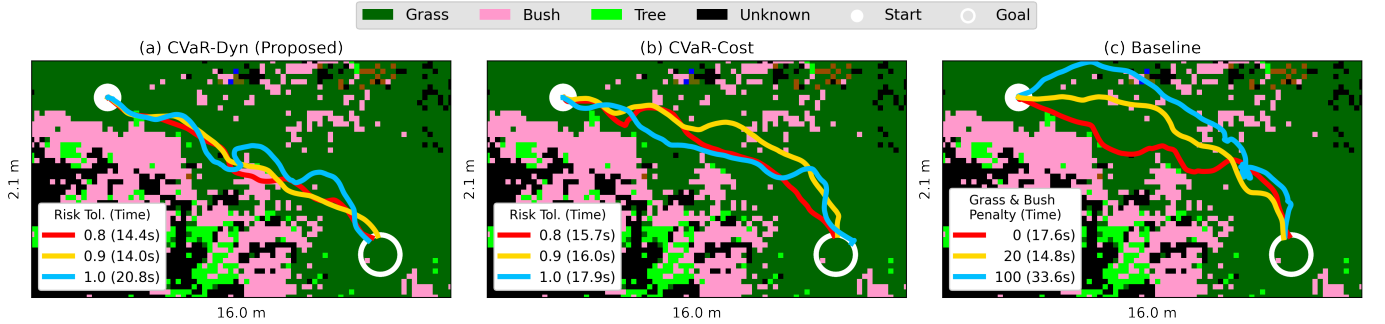


Fig. 21: Representative trials of the outdoor experiments. (a) The proposed CVaR-Dyn with  $\alpha < 1$  handled the noisy terrain traction well and produced less wavy trajectories compared to other methods. When  $\alpha = 1$  (WayFAST [27]), the expected traction provided a poor indication of the actual trajectory outcome, causing the constant correction in headings. (b) CVaR-Cost avoided the bushes and suffered from poor solutions due to reduced traction samples. (c) The baseline assumed nominal traction that led to under-steering. As soft penalties increased, the robot became more averse to tall grass and bushes. As most of the test area was filled with grass or bush, the baseline with large soft penalties struggled to find feasible plans to goal in subsequent trials.

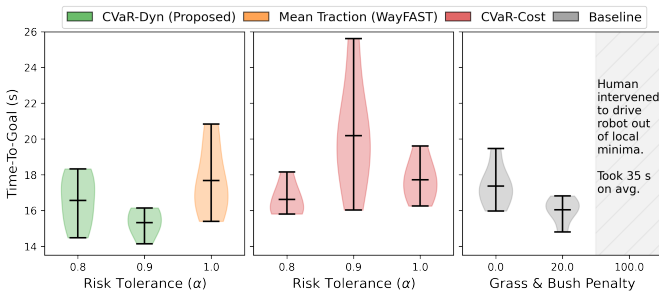


Fig. 22: The outdoor experiment results for benchmarking the local planners, where each planner completed 3 round trips or 6 trials in total. The proposed CVaR-Dyn with  $\alpha = 0.9$  outperformed CVaR-Cost that required more computation, WayFAST (CVaR-Dyn with  $\alpha = 1$ ) that planned with the expected traction, and the baseline that planned with the nominal traction and assigned soft penalties for grass and bushes.

distributions are selectively visualized in Fig. 20a to highlight multimodality. As shown in Fig. 20b, we chose 2 start-goal pairs for testing the planners and assessing the benefits of avoiding OOD terrain, respectively. All planners avoided the terrain with elevation greater than 1.4 m via auxiliary penalties, and the baseline assigned soft costs for the grass and bush semantic types with elevations less than 1.4 m. While the 1.4 m height threshold is much higher than the robot’s step height, the selected test environments did not have short

and rigid obstacles in order to analyze the planners’ ability to handle tall vegetation. The robot maintained a semantic octomap with 0.2 m resolution by fusing semantic pointclouds generated from projecting semantic images to lidar pointcloud for accurate depth. Due to limited GPU resources shared by semantic classification, traction prediction, and motion planning, the planners could only reliably plan at 5 Hz with 8 s look-ahead and 800 control rollouts, and CVaR-Cost was only allowed 200 traction map samples. The maximum linear and angular velocities were 1 m/s and 90 degree/s.

The results for the planner benchmark are summarized in Fig. 22, where we considered 3 round trips to and from the goal (6 trials in total) for each method. Qualitative visualizations are provided in Fig. 21. Overall, CVaR-Dyn with  $\alpha = 0.9$  achieved the best time-to-goal and success rate, consistent with the indoor experiments in Sec. IX-A. The CVaR-Cost planner was more conservative by staying far from the bushes. In comparison, the baseline and the CVaR-Dyn planner with  $\alpha = 1$  (WayFAST [27]) both suffered from noisy real-world traction, causing wide turns. Notably, when the soft penalty for grass and bush semantic types was too high, the baseline planner could not find any solution to the goal, thus requiring human interventions and long mission time.

The quantitative and qualitative results for the OOD avoid-



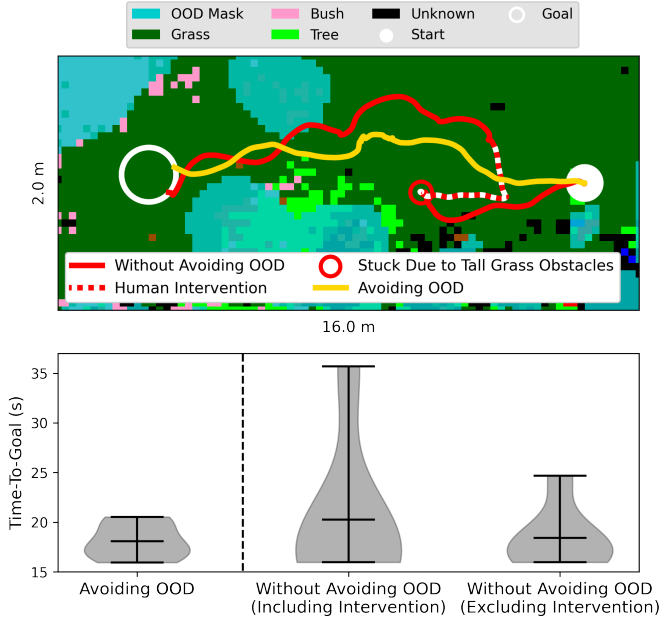


Fig. 23: Benefits of avoiding OOD terrain whose latent features have normalized densities below 0. The planners that avoided or did not avoid OOD terrain each completed 3 round trips or 6 trials in total. Without OOD avoidance, the robot was stuck in local minima due to imperfect online map and noisy terrain traction, requiring human interventions to teleoperate the robot to a region with feasible plans to goal. In contrast, assigning auxiliary penalties for OOD terrain made it easier for the planner to find trajectories to goal.

ance experiments are shown in Fig. 23, where we used CVaR-Dyn with  $\alpha = 0.9$  and executed 3 round trips. We considered the terrain as OOD if the normalized densities for the traction predictor’s latent features fell below 0 (i.e., less familiar than terrain traversed during training) based on empirical tuning. Without avoiding OOD terrain, the robot was more prone to getting stuck in local minima and required human interventions to drive to the robot to areas with feasible trajectories to goal. In contrast, the planner that avoided OOD terrain achieved better time-to-goal without requiring human interventions. This conclusion is also consistent with Fig. 16 in that avoiding OOD improves the success rate.

## X. CONCLUSION & FUTURE WORK

This work proposed an uncertainty-aware traction model based on evidential deep learning that captures the uncertain terrain traction via empirical distributions (aleatoric uncertainty) and identifies unreliable predictions based on the densities of the traction predictor’s latent features (epistemic uncertainty). By leveraging the proposed uncertainty-aware squared Earth Mover’s Distance loss, we improved the network’s prediction accuracy, OOD detection performance, and the downstream navigation performance. To handle aleatoric uncertainty, we proposed a risk-aware planner that simulates state trajectories based on the left-tail CVaR of the traction distributions. To handle epistemic uncertainty, we proposed to assign auxiliary costs to terrain whose latent features have low densities, leading to higher navigation success rates. The overall pipeline was analyzed via extensive simulations and hardware experiments, demonstrating improved navigation performance across different ground robotic platforms.

Many interesting research directions exist that may improve the proposed approach. Firstly, this work assumed access to empirically estimated traction distributions that may be difficult to obtain for high-dimensional input features such as RGB images, but methods exist that can learn distributions using a single sample or a few samples from the target distribution, e.g., [57], [58]. In addition, this work focused on 2D dynamical models, but more complex models with six degrees of freedom are needed for challenging navigation environments with dirt mounds [44] and large rocks [59]. In addition, learning a speed-dependent traction model may further improve navigation performance [20], but it is challenging to collect a rich enough dataset that covers the entire speed profile of the robot and a diverse set of terrain types. Therefore, designing an efficient information gathering algorithm for collecting training data is important for learning a reliable dynamical model, e.g., [49], [60]. While we used a semantic octomap [52] to obtain both the semantic and geometric information of the environment, computationally cheaper alternatives based on semantic elevation mapping [19], [61] can be used instead. Moreover, this work avoided OOD terrain in new environments, but online adaptation can be performed [21] when human supervision is available. Lastly, to improve the performance of the autonomy stack, the proposed approach can be paired with a global planner that can leverage far-field features to provide waypoints over a longer range [62].

## ACKNOWLEDGMENT

This research was sponsored by ARL grant W911NF-21-2-0150 and by ONR grant N00014-18-1-2832. The hardware experiment using the Spot robot was completed during Xiaoyi Cai’s internship at the Boston Dynamics AI Institute (BDAI). The authors thank Harrison Busa, Velin Dimitrov, Brennan Vanderlaan, and Leonor Feroselle from BDAI for their help on the Spot robot’s payload, and Brian Okorn and Surya Singh from BDAI for their feedback on the paper. The authors also thank Andrew Fishberg from MIT for his help on the RC car.

## APPENDIX A PROOF OF THEOREM 1

We proceed directly from the definition of UEMD<sup>2</sup> (19) and simplify the notation by making the expectation over  $\mathbf{p} \sim \text{Dir}(\beta)$  implicit. Recall that  $\mathbf{y}$  is the target PMF,  $\text{cs}(\cdot)$  is the cumulative sum operator, and we denote  $\text{cs}_b(\cdot)$  as the  $b$ -th entry



of the cumulative sum vector.

$$\text{UEMD}^2(\beta, \mathbf{y}) \quad (31)$$

$$:= \mathbb{E}[\text{EMD}^2(\mathbf{p}, \mathbf{y})] \quad (32)$$

$$= \mathbb{E}\left[\sum_{b=1}^B (\text{cs}_b(\mathbf{p}) - \text{cs}_b(\mathbf{y}))^2\right] \quad (33)$$

$$= \sum_{b=1}^B \mathbb{E}\left(\sum_{i=1}^b p_i - \sum_{i=1}^b y_i\right)^2 \quad (34)$$

$$= \sum_{b=1}^B \left[ \mathbb{E}\left(\sum_{i=1}^b p_i\right)^2 - 2 \underbrace{\mathbb{E}\sum_{i=1}^b p_i \sum_{i=1}^b y_i}_{\text{cs}_b(\mathbf{y})} + \underbrace{\mathbb{E}\left(\sum_{i=1}^b y_i\right)^2}_{\text{cs}_b(\mathbf{y})^2} \right] \quad (35)$$

After separating out the constant additive term  $\text{cs}_b(\mathbf{y})^2$ , expanding the remaining terms, and moving the expectation inside the summation, we obtain:

$$= \sum_{b=1}^B \left( \underbrace{\sum_{i=1}^b \mathbb{E}[p_i^2]}_{(a)} + 2 \sum_{1 \leq i < j \leq b} \underbrace{\mathbb{E}[p_i p_j]}_{(b)} - 2 \text{cs}_b(\mathbf{y}) \underbrace{\sum_{i=1}^b \mathbb{E}[p_i]}_{(c)} \right) + \text{cs}(\mathbf{y})^\top \text{cs}(\mathbf{y}) \quad (36)$$

The terms (a-c) in (36) can be easily derived in closed-form based on the standard properties of a Dirichlet distribution (namely, the variance, covariance and mean):

$$(a) \mathbb{E}[p_i^2] = \text{Var}(p_i) + \mathbb{E}[p_i]^2, \quad (37)$$

$$= \frac{\beta_i(\beta_0 - \beta_i)}{\beta_0^2(\beta_0 + 1)} + \frac{\beta_i^2}{\beta_0^2}, \quad (38)$$

$$= \frac{\beta_i + \beta_i^2}{\beta_0(\beta_0 + 1)}. \quad (39)$$

When  $i \neq j$ ,

$$(b) \mathbb{E}[p_i p_j] = \text{Cov}(p_i, p_j) + \mathbb{E}[p_i] \mathbb{E}[p_j], \quad (40)$$

$$= \frac{-\beta_i \beta_j}{\beta_0^2(\beta_0 + 1)} + \frac{\beta_i \beta_j}{\beta_0^2}, \quad (41)$$

$$= \frac{\beta_i \beta_j}{\beta_0(\beta_0 + 1)}. \quad (42)$$

Lastly, (c)  $\mathbb{E}[p_i] = \frac{\beta_i}{\beta_0}$ . Substituting (a-c) in (36), we obtain

$$= \sum_{b=1}^B \left( \sum_{i=1}^b \frac{\beta_i + \beta_i^2}{\beta_0(\beta_0 + 1)} + 2 \sum_{1 \leq i < j \leq b} \frac{\beta_i \beta_j}{\beta_0(\beta_0 + 1)} - 2 \text{cs}_b(\mathbf{y}) \sum_{i=1}^b \frac{\beta_i}{\beta_0} \right) + \text{cs}(\mathbf{y})^\top \text{cs}(\mathbf{y}), \quad (43)$$

$$= \frac{1}{\beta_0(\beta_0 + 1)} \sum_{b=1}^B \left( \sum_{i=1}^b \beta_i + \sum_{i=1}^b \beta_i^2 + 2 \sum_{1 \leq i < j \leq b} \beta_i \beta_j \right) - \frac{2}{\beta_0} \sum_{b=1}^B \left( \text{cs}_b(\mathbf{y}) \sum_{i=1}^b \beta_i \right) + \text{cs}(\mathbf{y})^\top \text{cs}(\mathbf{y}) \quad (44)$$

$$= \frac{1}{\beta_0(\beta_0 + 1)} \sum_{b=1}^B \left( \underbrace{\sum_{i=1}^b \beta_i}_{\text{cs}_b(\beta)} + \underbrace{\left(\sum_{i=1}^b \beta_i\right)^2}_{\text{cs}_b(\beta)^2} \right) - \frac{2}{\beta_0} \sum_{b=1}^B \left( \underbrace{\text{cs}_b(\mathbf{y}) \sum_{i=1}^b \beta_i}_{\text{cs}_b(\beta)} \right) + \text{cs}(\mathbf{y})^\top \text{cs}(\mathbf{y}) \quad (45)$$

$$= \frac{\text{cs}(\beta)^\top \text{cs}(\beta) + \mathbb{1}_B}{\beta_0(\beta_0 + 1)} - 2 \frac{\text{cs}(\beta)^\top}{\beta_0} \text{cs}(\mathbf{y}) + \text{cs}(\mathbf{y})^\top \text{cs}(\mathbf{y}), \quad (46)$$

$$= \text{cs}(\bar{\mathbf{p}})^\top \frac{\text{cs}(\beta) + \mathbb{1}_B}{\beta_0 + 1} + \eta(q, \mathbf{y}) \quad (47)$$

where  $\bar{\mathbf{p}} = \beta/\beta_0 = E_{\mathbf{p} \sim \text{Dir}(\beta)}[\mathbf{p}]$  and  $\eta$  is defined in (18).  $\square$

## REFERENCES

- [1] B. Charpentier, O. Borchert, D. Zügner, S. Geisler, and S. Günnemann, "Natural Posterior Network: Deep Bayesian Predictive Uncertainty for Exponential Family Distributions," in *International Conference on Learning Representations*, 2022.
- [2] I. Kobyzev, S. J. Prince, and M. A. Brubaker, "Normalizing flows: An introduction and review of current methods," *IEEE Transactions on Pattern Analysis and Machine Intelligence*, vol. 43, no. 11, pp. 3964–3979, 2021.
- [3] G. Williams, N. Wagener, B. Goldfain, P. Drews, J. M. Rehg, B. Boots, and E. A. Theodorou, "Information theoretic mpc for model-based reinforcement learning," in *2017 IEEE International Conference on Robotics and Automation (ICRA)*. IEEE, 2017, pp. 1714–1721.
- [4] J. A. Bagnell, D. Bradley, D. Silver, B. Sofman, and A. Stentz, "Learning for autonomous navigation," *IEEE Robotics & Automation Magazine*, vol. 17, no. 2, pp. 74–84, 2010.
- [5] D. Silver, J. A. Bagnell, and A. Stentz, "Learning from demonstration for autonomous navigation in complex unstructured terrain," *The International Journal of Robotics Research*, vol. 29, no. 12, pp. 1565–1592, 2010.
- [6] D. D. Fan, K. Otsu, Y. Kubo, A. Dixit, J. Burdick, and A.-A. Agha-Mohammadi, "Step: Stochastic traversability evaluation and planning for risk-aware off-road navigation," in *Robotics: Science and Systems*. RSS Foundation, 2021, pp. 1–21.
- [7] F. Ruetz, N. Lawrance, E. Hernández, P. Borges, and T. Peynot, "Forest-trav: Accurate, efficient and deployable forest traversability estimation for autonomous ground vehicles," *arXiv preprint arXiv:2305.12705*, 2023.
- [8] J. Frey, D. Hoeller, S. Khattak, and M. Hutter, "Locomotion policy guided traversability learning using volumetric representations of complex environments," *arXiv preprint arXiv:2203.15854*, 2022.
- [9] X. Meng, N. Hatch, A. Lambert, A. Li, N. Wagener, M. Schmittle, J. Lee, W. Yuan, Z. Chen, S. Deng, *et al.*, "Terrainnet: Visual modeling of complex terrain for high-speed, off-road navigation," *arXiv preprint arXiv:2303.15771*, 2023.

- [10] A. Shaban, X. Meng, J. Lee, B. Boots, and D. Fox, "Semantic terrain classification for off-road autonomous driving," in *Conference on Robot Learning*. PMLR, 2022, pp. 619–629.
- [11] A. Valada, G. Oliveira, T. Brox, and W. Burgard, "Deep multispectral semantic scene understanding of forested environments using multimodal fusion," in *International Symposium on Experimental Robotics (ISER)*, 2016.
- [12] A. Valada, J. Vertens, A. Dhall, and W. Burgard, "Adapnet: Adaptive semantic segmentation in adverse environmental conditions," in *2017 IEEE International Conference on Robotics and Automation (ICRA)*. IEEE, 2017, pp. 4644–4651.
- [13] Z. Chen, D. Pushp, and L. Liu, "Cali: Coarse-to-fine alignments based unsupervised domain adaptation of traversability prediction for deployable autonomous navigation," *arXiv preprint arXiv:2204.09617*, 2022.
- [14] T. Guan, D. Kothandaraman, R. Chandra, A. J. Sathiyamoorthy, K. Weerakoon, and D. Manocha, "Ga-nav: Efficient terrain segmentation for robot navigation in unstructured outdoor environments," *IEEE Robotics and Automation Letters*, vol. 7, no. 3, pp. 8138–8145, 2022.
- [15] T. Guan, Z. He, R. Song, D. Manocha, and L. Zhang, "Tns: Terrain traversability mapping and navigation system for autonomous excavators," *Robotics: Science and Systems XVIII*, 2021.
- [16] G. Kahn, P. Abbeel, and S. Levine, "Badgr: An autonomous self-supervised learning-based navigation system," *IEEE Robotics and Automation Letters*, vol. 6, no. 2, pp. 1312–1319, 2021.
- [17] X. Yao, J. Zhang, and J. Oh, "Rca: Ride comfort-aware visual navigation via self-supervised learning," *arXiv preprint arXiv:2207.14460*, 2022.
- [18] J. Zörn, W. Burgard, and A. Valada, "Self-supervised visual terrain classification from unsupervised acoustic feature learning," *IEEE Transactions on Robotics*, vol. 37, no. 2, pp. 466–481, 2020.
- [19] P. Ewen, A. Li, Y. Chen, S. Hong, and R. Vasudevan, "These maps are made for walking: Real-time terrain property estimation for mobile robots," *IEEE Robotics and Automation Letters*, vol. 7, no. 3, pp. 7083–7090, 2022.
- [20] X. Cai, M. Everett, J. Fink, and J. P. How, "Risk-aware off-road navigation via a learned speed distribution map," in *2022 IEEE/RSJ International Conference on Intelligent Robots and Systems (IROS)*. IEEE, 2022, pp. 2931–2937.
- [21] J. Frey, M. Mattamala, N. Chebrolu, C. Cadena, M. Fallon, and M. Hutter, "Fast Traversability Estimation for Wild Visual Navigation," in *Proceedings of Robotics: Science and Systems*, Daegu, Republic of Korea, July 2023.
- [22] R. Schmid, D. Atha, F. Schöller, S. Dey, S. Fakoorian, K. Otsu, B. Ridge, M. Bjelonic, L. Wellhausen, M. Hutter, *et al.*, "Self-supervised traversability prediction by learning to reconstruct safe terrain," in *2022 IEEE/RSJ International Conference on Intelligent Robots and Systems (IROS)*. IEEE, 2022, pp. 12 419–12 425.
- [23] H. Lee, J. Kwon, and C. Kwon, "Learning-based uncertainty-aware navigation in 3d off-road terrains," in *2023 IEEE International Conference on Robotics and Automation (ICRA)*. IEEE, 2023, pp. 10 061–10 068.
- [24] M. Endo, T. Tani, R. Yonetani, and G. Ishigami, "Risk-aware path planning via probabilistic fusion of traversability prediction for planetary rovers on heterogeneous terrains," *arXiv preprint arXiv:2303.01169*, 2023.
- [25] L. Hou, C.-P. Yu, and D. Samaras, "Squared earth mover's distance-based loss for training deep neural networks," *arXiv preprint arXiv:1611.05916*, 2016.
- [26] K. P. Murphy, *Machine learning: a probabilistic perspective*. MIT press, 2012.
- [27] M. V. Gasparino, A. N. Sivakumar, Y. Liu, A. E. B. Velasquez, V. A. H. Higuti, J. Rogers, H. Tran, and G. Chowdhary, "Wayfast: Navigation with predictive traversability in the field," *IEEE Robotics and Automation Letters*, vol. 7, no. 4, pp. 10 651–10 658, 2022.
- [28] Z. Wang, O. So, K. Lee, and E. A. Theodorou, "Adaptive risk sensitive model predictive control with stochastic search," in *Learning for Dynamics and Control*. PMLR, 2021, pp. 510–522.
- [29] F. G. Oliveira, A. A. Neto, D. Howard, P. Borges, M. F. Campos, and D. G. Macharet, "Three-dimensional mapping with augmented navigation cost through deep learning," *Journal of Intelligent & Robotic Systems*, vol. 101, no. 3, pp. 1–21, 2021.
- [30] S. Otte, C. Weiss, T. Scherer, and A. Zell, "Recurrent neural networks for fast and robust vibration-based ground classification on mobile robots," in *2016 IEEE International Conference on Robotics and Automation (ICRA)*. IEEE, 2016, pp. 5603–5608.
- [31] T. Overbye and S. Saripalli, "G-vom: A gpu accelerated voxel off-road mapping system," in *2022 IEEE Intelligent Vehicles Symposium (IV)*. IEEE, 2022, pp. 1480–1486.
- [32] A. Jagan Sathiyamoorthy, K. Weerakoon, T. Guan, M. Russell, D. Conover, J. Pusey, and D. Manocha, "Vern: Vegetation-aware robot navigation in dense unstructured outdoor environments," *arXiv e-prints*, pp. arXiv–2303, 2023.
- [33] T. Guan, Z. He, D. Manocha, and L. Zhang, "Ttm: Terrain traversability mapping for autonomous excavator navigation in unstructured environments," *arXiv preprint arXiv:2109.06250*, 2021.
- [34] Y. Tan, N. Virani, B. Good, S. Gray, M. Youssefhussein, Z. Yang, K. Angelis, N. Abate, and S. Sen, "Risk-aware autonomous navigation," in *Artificial Intelligence and Machine Learning for Multi-Domain Operations Applications III*, vol. 11746. International Society for Optics and Photonics, 2021, p. 117461D.
- [35] P. Papadakis, "Terrain traversability analysis methods for unmanned ground vehicles: A survey," *Engineering Applications of Artificial Intelligence*, vol. 26, no. 4, pp. 1373–1385, 2013.
- [36] A. Li, C. Yang, J. Frey, J. Lee, C. Cadena, and M. Hutter, "Seeing through the grass: Semantic pointcloud filter for support surface learning," *arXiv preprint arXiv:2305.07995*, 2023.
- [37] J. Seo, S. Sim, and I. Shim, "Learning off-road terrain traversability with self-supervisions only," *IEEE Robotics and Automation Letters*, 2023.
- [38] J. Seo, T. Kim, K. Kwak, J. Min, and I. Shim, "Scate: A scalable framework for self-supervised traversability estimation in unstructured environments," *IEEE Robotics and Automation Letters*, vol. 8, no. 2, pp. 888–895, 2023.
- [39] L. Murphy, S. Martin, and P. Corke, "Creating and using probabilistic costmaps from vehicle experience," in *2012 IEEE/RSJ International Conference on Intelligent Robots and Systems*. IEEE, 2012, pp. 4689–4694.
- [40] D. D. Fan, A.-A. Agha-Mohammadi, and E. A. Theodorou, "Learning risk-aware costmaps for traversability in challenging environments," *IEEE Robotics and Automation Letters*, vol. 7, no. 1, pp. 279–286, 2021.
- [41] S. Triest, M. G. Castro, P. Maheshwari, M. Sivaprakasam, W. Wang, and S. Scherer, "Learning risk-aware costmaps via inverse reinforcement learning for off-road navigation," *arXiv preprint arXiv:2302.00134*, 2023.
- [42] A. Majumdar and M. Pavone, "How should a robot assess risk? towards an axiomatic theory of risk in robotics," in *Robotics Research*. Springer, 2020, pp. 75–84.
- [43] J. Gibson, B. Vlahov, D. Fan, P. Spieler, D. Pastor, A.-a. Agha-mohammadi, and E. A. Theodorou, "A multi-step dynamics modeling framework for autonomous driving in multiple environments," in *2023 IEEE International Conference on Robotics and Automation (ICRA)*, 2023, pp. 7959–7965.
- [44] H. Lee, T. Kim, J. Mun, and W. Lee, "Learning terrain-aware kinodynamic model for autonomous off-road rally driving with model predictive path integral control," *IEEE Robotics and Automation Letters*, vol. 8, no. 11, pp. 7663–7670, 2023.
- [45] K. Chua, R. Calandra, R. McAllister, and S. Levine, "Deep reinforcement learning in a handful of trials using probabilistic dynamics models," *Advances in neural information processing systems*, vol. 31, 2018.
- [46] J. Gawlikowski, C. R. N. Tassi, M. Ali, J. Lee, M. Humt, J. Feng, A. Kruspe, R. Triebel, P. Jung, R. Roscher, *et al.*, "A survey of uncertainty in deep neural networks," *arXiv preprint arXiv:2107.03342*, 2021.
- [47] Y. Gal and Z. Ghahramani, "Dropout as a bayesian approximation: Representing model uncertainty in deep learning," in *international conference on machine learning*. PMLR, 2016, pp. 1050–1059.
- [48] I. Osband, C. Blundell, A. Pritzel, and B. Van Roy, "Deep exploration via bootstrapped dqn," *Advances in neural information processing systems*, vol. 29, 2016.
- [49] T. Kim, J. Mun, J. Seo, B. Kim, and S. Hong, "Bridging Active Exploration and Uncertainty-Aware Deployment Using Probabilistic Ensemble Neural Network Dynamics," in *Robotics: Science and Systems (RSS)*, July 2023.
- [50] B. Lakshminarayanan, A. Pritzel, and C. Blundell, "Simple and scalable predictive uncertainty estimation using deep ensembles," *Advances in neural information processing systems*, vol. 30, 2017.
- [51] X. Cai, M. Everett, L. Sharma, P. R. Osteen, and J. P. How, "Probabilistic traversability model for risk-aware motion planning in off-road environments," in *2023 IEEE/RSJ International Conference on Intelligent Robots and Systems (IROS)*, 2023.
- [52] A. Asgharivaskasi and N. Atanasov, "Active bayesian multi-class mapping from range and semantic segmentation observations," in *2021 IEEE International Conference on Robotics and Automation (ICRA)*. IEEE, 2021, pp. 1–7.

- [53] A. Kirillov, Y. Wu, K. He, and R. Girshick, "Pointrend: Image segmentation as rendering," in *Proceedings of the IEEE/CVF conference on computer vision and pattern recognition*, 2020, pp. 9799–9808.
- [54] M. Wigness, S. Eum, J. G. Rogers, D. Han, and H. Kwon, "A rugd dataset for autonomous navigation and visual perception in unstructured outdoor environments," in *International Conference on Intelligent Robots and Systems (IROS)*, 2019.
- [55] D. Rezende and S. Mohamed, "Variational inference with normalizing flows," in *International conference on machine learning*. PMLR, 2015, pp. 1530–1538.
- [56] T. Kim, G. Park, K. Kwak, J. Bae, and W. Lee, "Smooth model predictive path integral control without smoothing," *IEEE Robotics and Automation Letters*, vol. 7, no. 4, pp. 10 406–10 413, 2022.
- [57] H. Su, C. R. Qi, Y. Li, and L. J. Guibas, "Render for cnn: Viewpoint estimation in images using cnns trained with rendered 3d model views," in *Proceedings of the IEEE international conference on computer vision*, 2015, pp. 2686–2694.
- [58] T. Hospedales, A. Antoniou, P. Micaelli, and A. Storkey, "Meta-learning in neural networks: A survey," *IEEE transactions on pattern analysis and machine intelligence*, vol. 44, no. 9, pp. 5149–5169, 2021.
- [59] A. Datar, C. Pan, and X. Xiao, "Learning to model and plan for wheeled mobility on vertically challenging terrain," *arXiv preprint arXiv:2306.11611*, 2023.
- [60] M. Endo and G. Ishigami, "Active traversability learning via risk-aware information gathering for planetary exploration rovers," *IEEE Robotics and Automation Letters*, vol. 7, no. 4, pp. 11 855–11 862, 2022.
- [61] G. Erni, J. Frey, T. Miki, M. Mattamala, and M. Hutter, "Mem: Multi-modal elevation mapping for robotics and learning," *arXiv preprint arXiv:2309.16818*, 2023.
- [62] E. Chen, C. Ho, M. Maulimov, C. Wang, and S. Scherer, "Learning-on-the-drive: Self-supervised adaptation of visual offroad traversability models," *arXiv preprint arXiv:2306.15226*, 2023.